Electronic Supplementary Material (ESI) for Chemical Science.
This journal is © The Royal Society of Chemistry 2022

Electronic Supplementary Information

One-electron Bonds in Copper-Aluminum and Copper-Gallium Complexes

Brendan J. Graziano[†], *Thais R. Scott*[‡], *Matthew V. Vollmer*[†], *Michael J. Dorantes*[†], *Victor G. Young Jr.*[†], *Eckhard Bill*[§,*], *Laura Gagliardi*[‡,*], *and Connie C. Lu*[†,◊,*]

[†]Department of Chemistry, University of Minnesota-Twin Cities, 207 Pleasant Street SE, Minneapolis, Minnesota 55455, United States

[‡]Department of Chemistry, The University of Chicago, Searle Chemistry Laboratory 5735 South Ellis Avenue, Chicago, Illinois 60637, United States

[§]Max Planck Institut für Chemische Energiekonversion, Stiftstraße 34–36, 45470 Mülheim an der Ruhr, Germany

[◊]Institut für Anorganische Chemie, Rheinische-Friedrich-Wilhelms Universität Bonn, Gerhard-Domagk-Straße 1, 53121 Bonn, Germany

*corresponding authors' e-mails: eckhard.bill@cec.mpg.de, lgagliardi@uchicago.edu, clu@uni-bonn.de

ESI Table of Contents

Experimental Section

General Considerations. Unless otherwise stated, all manipulations were performed under a purified Ar atmosphere using standard Schlenk techniques or an inert atmosphere glovebox with < 1.0 ppm O_2 and H_2O. Standard solvents were deoxygenated by sparging with N_2 and dried by passing through activated alumina columns of an SG Water solvent purification system under Ar. Deuterated solvents were purchased from Cambridge Isotope Laboratories, Inc., degassed via freeze-pump-thaw cycles, and stored over activated 4 Å molecular sieves. THF-d_8 was dried over NaK, freeze-pump-thawed, and vacuum transferred into a Schlenk flask filled with ca. 20% w/v sieves. Fluorobenzene and 1,5-cyclooctadiene (abbreviated 1,5-COD) were purchased from Oakwood Chemicals, Inc. and MilliporeSigma respectively. These solvents were subsequently dried over CaH_2, distilled, then freeze-pump-thawed, and likewise stored over activated 4 Å molecular sieves. CuBr was purchased from Strem Chemicals, Inc. and used as received. All other reagents were purchased from commercial vendors and used without purification unless otherwise noted. All NMR spectra were recorded on Bruker 400 MHz spectrometer unless otherwise noted. Perpendicular-mode X-band EPR spectra were recorded at low (20 to 45 K) or ambient (298 K) temperature with a Bruker ESP 300 spectrometer equipped with an Oxford ESR 910 liquid-helium cryostat and an Oxford Instruments temperature controller. All spectra were collected using a modulation frequency of 100 kHz. EPR spectra were simulated utilizing Easyspin with the functions pepper (frozen solution) and garlic (fluid state) and refined using esfit until a satisfactory model was obtained.[1] Cyclic voltammetry was conducted using a CH Instruments 600 electrochemical analyzer. The one-cell setup utilized a glassy carbon working electrode, platinum wire counter electrode, and silver wire auxiliary electrode. Analyte solutions were prepared in a THF solution of 0.1 M $[^nPr_4N]BAr^F_4$ electrolyte (BAr^F_4 = tetrakis(3,5-bis(trifluoromethyl)phenyl)borate)) and referenced internally to the $FeCp_2/FeCp_2^+$ redox couple. UV–vis spectra were reocrded using glass cuvettes on a Varian Cary 300 Bio spectrophotometer. NMR shifts were referenced to the internal solvent residual signal (for ^1H spectra) or an external H_3PO_4 reference (for ^{31}P spectra). The neutral ligand $(N(o\text{-}(NHCH_2P^iPr_2)C_6H_4)_3$ (abbreviated as LH_3)[2], metalloligands $M(N(o\text{-}(NCH_2P^iPr_2)C_6H_4)_3$ (abbreviated ML, M = Al and Ga)[3], $[^nPr_4N]BAr^F_4$[4], mesitylcopper (abbreviated $(CuMes)_5$)[5], $[H(OEt_2)_2]BAr^F_4$[6], $Ag_2B_{12}Cl_{12}$[7], and KC_8[8] were prepared according to literature procedures. Elemental analyses were performed by Robertson Microlit Laboratories, Inc. (Ledgewood, NJ).

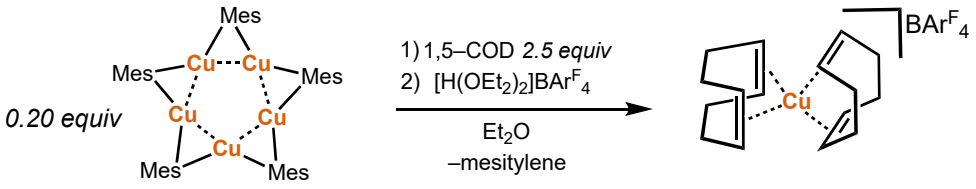

Synthesis of [Cu(C$_8$H$_{12}$)$_2$][B(3,5-(CF$_3$)$_2$C$_6$H$_3$)$_4$], [Cu(COD)$_2$]BAr$^F_4$: A mixture of (CuMes)$_5$ (0.200 g, 0.219 mmol) and 1,5-COD (336 µL, 2.736 mmol) in Et$_2$O (10 mL) was stirred and then cooled to −78 ˚C. To this mixture was added [H(OEt$_2$)$_2$]BAr$^F_4$ (1.108 g, 1.095 mmol) in 2 mL of Et$_2$O resulting in flashes of orange color that quickly dissipated. The solution was then stirred at room temperature for 3 h to give a translucent solution with a small amount of yellow precipitate (likely trace {Cu(COD)Cl}$_2$). The volume was reduced to ca. 2 mL, filtered through Celite and layered with 10 mL hexanes inducing the formation of a biphasic solution. Shaking the mixture resulted in precipitation of the product as a bright white crystalline solid. The solid was isolated by decanting the mother liquor, washed with hexanes (3 × 2 mL), and dried to afford 1.05 g (84% yield) of [Cu(COD)$_2$]BAr$^F_4$ as a white crystalline solid. Recrystallization was achieved by layering concentrated Et$_2$O solutions with hexanes. Crystals grown in this manner were suitable for X-ray diffraction. ^{1}H NMR (ppm, THF-*d*$_8$, 400 MHz): 7.79 (s, 8H, BAr$^F_4$ aryl), 7.58 (s, 4H, BAr$^F_4$ aryl), 5.69 (s, 8H, COD CH), 2.38 (s, 16H, COD CH$_2$). ^{13}C{^{1}H} NMR (ppm, THF-*d*$_8$, 101 MHz): 162.9 (C3), 136.7 (C4), 125.5 (q, $J_{C\text{-}F}$ = 282 Hz, C7), 118.2 (C6), 123.8 (C1), 28.9 (C2). The quaternary aryl carbon attached to CF$_3$ was not located. ^{19}F{^{1}H} NMR (ppm, THF-*d*$_8$, 376 MHz): –63.4. ^{11}B NMR (ppm, THF-*d*$_8$, 128 MHz): –6.5. Anal. calcd for **[Cu(COD)$_2$]**BAr$^F_4$, C$_{48}$H$_{36}$BF$_{24}$Cu (%): C, 50.43; H, 3.17. Found: C, 50.39; H, 3.11.

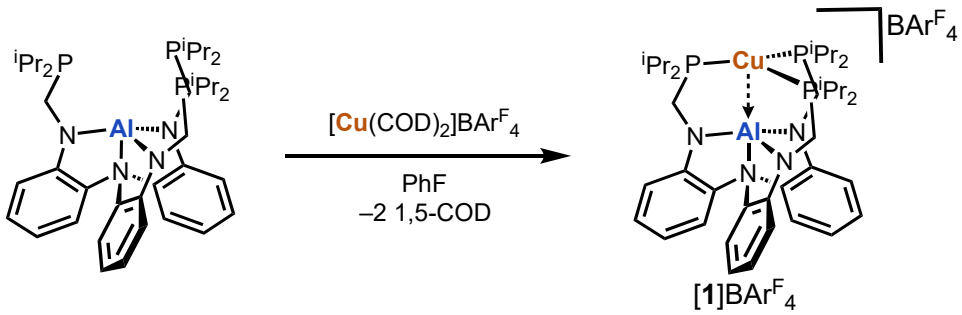

Synthesis of [CuAl(N(*o*-(NCH$_2$P^{i}Pr$_2$)C$_6$H$_4$)$_3$)][B(3,5-(CF$_3$)$_2$C$_6$H$_3$)$_4$], ([**1**]BAr$^F_4$): To a stirring solution of AlL (100 mg, 0.142 mmol, 4 mL fluorobenzene) was added a solution of [Cu(COD)$_2$]BAr$^F_4$ (162.2 mg 0.142 mmol, 2 mL fluorobenzene), which immediately gave rise to a bright yellow solution. The mixture was stirred for 3 h at room temperature, and then the volatiles were removed *in vacuo*. The resulting solids were triturated with 1:1 Et$_2$O:C$_6$H$_6$, washed with 5 mL of pentane, and dried to give 209 mg (90%) of [**1**]BAr$^F_4$ as a bright yellow powder. ^{1}H NMR

(ppm, C_6D_6, 400 MHz): 8.39 (s, 8H, $BAr^F{}_4$ aryl), 7.72 (s, 4H, $BAr^F{}_4$ aryl), 7.30 (d, $^3J_{H-H}$ = 10.0 Hz, 3H, aryl), 7.08 (t, $^3J_{H-H}$ = 7.5 Hz, 3H, aryl), 6.53 (t, $^3J_{H-H}$ = 7.5 Hz, 3H, aryl), 6.35 (d, $^3J_{H-H}$ = 5.0 Hz, 3H, aryl), 2.99 (br s, 6H, CH_2), 1.88 (br, 6H, PC*H*$(CH_3)_2$), 1.00–0.50 (m, 36H, PCH(C*H*$_3)_2$). $^{13}C\{^1H\}$ NMR (ppm, C_6D_6, 101 MHz): 162.8 (C10), 150.4 (C6), 135.1 (C11), 133.2 (C1), 129.0 (C4), 125.5 (C2), 125.1 (C14), 117.4 (C13), 117.1 (C3), 111.2 (C5), 44.0 (C7), 17.9 (C9). The quaternary aryl carbon attached to CF_3 (C12) and isopropyl methine (C8) were not located. ^{31}P NMR (162 MHz, C_6D_6): δ 16.9. $^{19}F\{^1H\}$ NMR (ppm, C_6D_6, 376 MHz): –62.1. ^{11}B NMR (ppm, C_6D_6, 128 MHz): –5.9. Anal. calcd for **1**, $C_{71}H_{72}N_4P_3BF_{24}AlCu$ (%): C, 52.27; H, 4.45; N, 3.43. Found: C, 50.65; H, 4.28; N, 3.39. Anal. calcd for [**1**]$BAr^F{}_4$•3O, $C_{71}H_{72}N_4P_3O_3BF_{24}AlCu$ (%): C, 50.77; H, 4.32; N, 3.34. Elemental analysis is consistent with oxidation of all three phosphines.

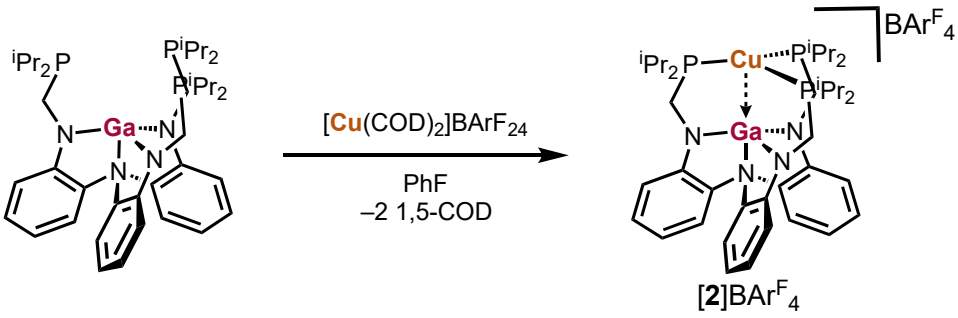

Synthesis of [CuGa(N(*o*-(NCH$_2$P^{i}Pr$_2$)C$_6$H$_4$)$_3$)][B(3,5-(CF$_3$)$_2$C$_6$H$_3$)$_4$], ([**2**]$BAr^F{}_4$): To a stirring solution of GaL (100 mg, 0.134 mmol, 4 mL fluorobenzene) was added a solution of [**Cu(COD)$_2$**]$BAr^F{}_4$ (152.9 mg, 0.134 mmol, 2 mL fluorobenzene), which immediately gave rise to a bright orange solution. The mixture was stirred for 3 h at room temperature and the volatiles were removed *in vacuo*. The resulting solid was triturated with 1:1: Et_2O:C_6H_6, washed with 5 mL of pentane, and dried to give 210 mg (94%) of [**2**]$BAr^F{}_4$ as vibrant orange powder. ^1H NMR (ppm, C_6D_6, 400 MHz): 8.38 (s, 8H, $BAr^F{}_4$ aryl), 7.72 (s, 4H, $BAr^F{}_4$ aryl), 7.36 (d, $^3J_{H-H}$ = 10.0 Hz, 3H, aryl), 7.08 (t, $^3J_{H-H}$ = 10.0 Hz, 3H, aryl), 6.53 (t, $^3J_{H-H}$ = 7.5 Hz, 3H, aryl), 6.34 (d, $^3J_{H-H}$ = 10.0 Hz, 3H, aryl), 3.10 (s, 6H, CH_2), 1.88 (br, 6H, PC*H*$(CH_3)_2$), 0.80–0.50 (m, 36H, PCH(C*H*$_3)_2$). $^{13}C\{^1H\}$ NMR (ppm, C_6D_6, 101 MHz): 162.6 (C10), 149.7 (C6), 135.2 (C11), 133.0 (C1), 128.7 (C4), 126.1 (C2), 125.3 (C14), 117.4 (C13), 116.8 (C3), 111.0 (C5), 44.6 (C7), 17.9 (C9). The quaternary aryl carbon attached to CF_3 (C12) and isopropyl methine carbon (C8) were not located. ^{31}P NMR (162 MHz, C_6D_6): δ 22.4. $^{19}F\{^1H\}$ NMR (ppm, C_6D_6, 376 MHz): –62.1. ^{11}B NMR (ppm, C_6D_6, 128 MHz): –5.9. Anal. calcd for [**2**]$BAr^F{}_4$, $C_{71}H_{72}N_4P_3BF_{24}GaCu$ (%): C, 50.93; H, 4.33; N, 3.35. Found: C, 51.11; H, 4.45; N, 3.21.

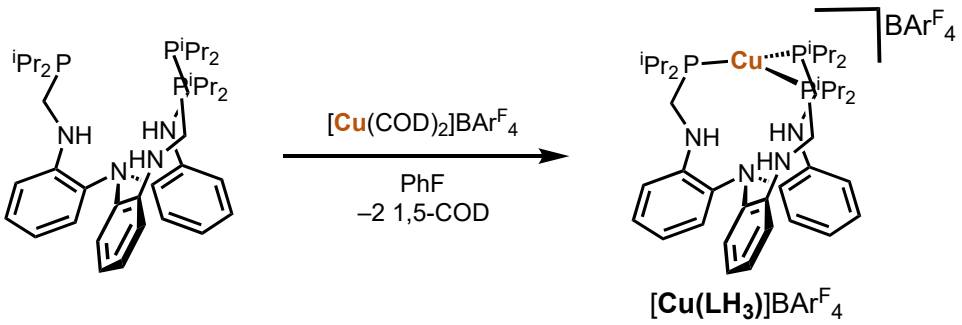

Synthesis of [Cu(N(*o*-(NCH$_2$P^{i}Pr$_2$)C$_6$H$_4$)$_3$)][B(3,5-(CF$_3$)$_2$C$_6$H$_3$)$_4$], ([**Cu(LH$_3$)**]BAr$^F_4$): To a stirring solution of LH$_3$ (100 mg, 0.147 mmol, 4 mL fluorobenzene) was added a solution of [**Cu(COD)$_2$**]BAr$^F_4$ (167.9 mg, 0.147 mmol, 2 mL fluorobenzene). The mixture was stirred for 3 h at room temperature and the volatiles were removed *in vacuo*. The resulting solid was triturated with 1:1: Et$_2$O:C$_6$H$_6$, washed with 5 mL of pentane, and dried to give 188 mg (80%) of [**Cu(LH$_3$)**]BAr$^F_4$ as a white powder. ^{1}H NMR (ppm, THF-d_8, 400 MHz): 7.79 (s, 8H, BAr$^F_4$ aryl), 7.57 (s, 4H, BAr$^F_4$ aryl), 7.09–7.05 (m, 6H, aryl), 6.76 (d, $^3J_{H-H}$ = 8.0 Hz, 3H, aryl), 6.70 (t, $^3J_{H-H}$ = 6.0 Hz, 3H, aryl), 4.57 (m, 3H, NH), 3.55 (br, 6H, CH$_2$), 2.39 (br, 6H, PC*H*(CH$_3$)$_2$), 1.47–0.97 (br, 36H, PCH(C*H*$_3$)$_2$). ^{13}C{^{1}H} NMR (ppm, C$_6$D$_6$, 101 MHz): 142.8 (C6), 134.2 (C11), 132.2 (C1), 126.7 (C4), 126.0 (C2), 124.2 (C14), 118.0 (C3), 116.8 (C13), 111.6 (C5), 40.5 (C7). The quaternary aryl carbon attached to CF$_3$ (C12), quaternary aryl carbon attached to B (C10), and isopropyl methine carbon (C8) were not located. ^{31}P NMR (162 MHz, C$_6$D$_6$): δ 16.5. ^{19}F{^{1}H} NMR (ppm, C$_6$D$_6$, 376 MHz): –63.4. ^{11}B NMR (ppm, C$_6$D$_6$, 128 MHz): –6.5. Anal. calcd for [**Cu(LH$_3$)**]BAr$^F_4$, C$_{71}$H$_{75}$N$_4$P$_3$BF$_{24}$Cu (%): C, 53.05; H, 4.70; N, 3.49. Found: C, 53.26; H, 4.84; N, 3.32.

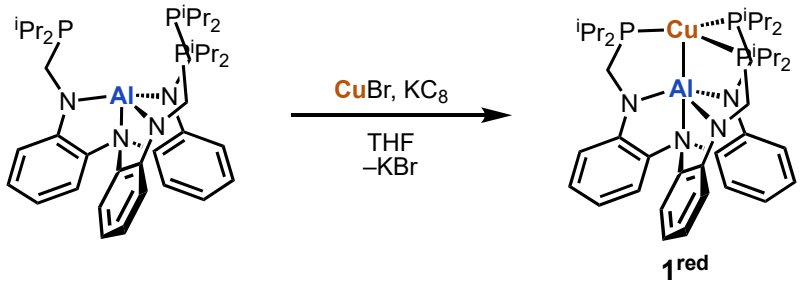

Synthesis of CuAl(N(*o*-(NCH$_2$P^{i}Pr$_2$)C$_6$H$_4$)$_3$), CuAlL (1^{red}): To a solution of AlL (100 mg, 0.142 mmol, 10 mL THF) was added a slurry of CuBr (20.4 mg, 0.142 mmol, 2 mL THF) giving a pale-yellow suspension. Once full consumption of CuBr was observed (ca. 1 h), KC$_8$ (19.2 mg, 0.142 mmol) was added all at once, causing the solution color to become dark maroon. The solution was stirred for 1 h, filtered through Celite, and then reduced to dryness *in vacuo*. Trituration with benzene (3 mL) afforded 77.5 mg (71% yield) of a maroon flaky solid. No distinct ^{1}H NMR resonances were observed, so **1^{red}** was characterized by EPR spectroscopy. X-ray quality crystals

were grown from concentrated Et_2O solutions at –30 °C resulting in the solvate **1**^{red} • $C_4H_{10}O$. Anal. calcd for **1**^{red}, $C_{39}H_{60}N_4P_3AlCu$ (%): C, 60.96; H, 7.87; N, 7.29. Found: C, 60.90; H, 7.84; N, 7.26.

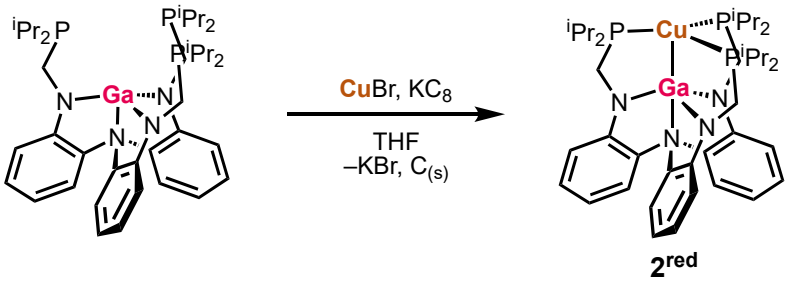

2^{red}

Synthesis of CuGa(N(*o*-(NCH$_2$P^{i}Pr$_2$)C$_6$H$_4$)$_3$), CuGaL (2^{red}): To a solution of GaL (100 mg, 0.134 mmol, 10 mL THF) was added a slurry of CuBr (19.2 mg, 0.134 mmol, 2 mL THF) giving a pale-yellow suspension. Once full consumption of CuBr was observed (ca. 1 h), KC_8 (18.1 mg, 0.134 mmol) was added all at once, causing the solution to become deep red. The solution was stirred for 1 h, filtered through Celite, and then reduced to dryness *in vacuo*. Trituration with benzene (3 mL) afforded 70.5 mg (65% yield) of a red flaky solid. No distinct ^{1}H NMR resonances were observed, so **2**^{red} was characterized by EPR spectroscopy. X-ray quality crystals were grown from vapor diffusion of pentane into a concentrated toluene solution at room temperature resulting the solvate **2**^{red} • C_7H_8. Anal. calcd for **2**^{red}, $C_{39}H_{60}N_4P_3GaCu$ (%): C, 57.75; H, 7.46; N, 6.91. Found: C, 60.89; H, 7.41; N, 6.08. Anal. calcd for **2**^{red} • C_7H_8, $C_{46}H_{68}N_4P_3GaCu$ (%): C, 61.17; H, 7.59; N, 6.20.

General procedure for the oxidation of CuML to obtain crystalline [CuML]$_2$[B$_{12}$Cl$_{12}$] salts: Complexes **1**^{red} or **2**^{red} (20 mg,) were dissolved in THF (ca. 0.5 mL) and transferred to an NMR tube. Likewise, a solution of $Ag_2[B_{12}Cl_{12}]$ (1.1 equiv. relative to the bimetallic, ca. 1 mL THF) was also prepared and carefully layered on top of the bimetallic solution in the NMR tube. The layering was placed in a covered container to protect from light and allowed to diffuse for 3 days, after which small yellow ([**1**]$_2$[B$_{12}$Cl$_{12}$]) or orange ([**2**]$_2$[B$_{12}$Cl$_{12}$]) blocks were deposited on the walls of the tube. The crystals were carefully isolated from the mixture and analyzed by X-ray diffraction. Spectroscopic characterization of these species are identical to those presented above for [**1**]BAr$^F{}_4$ or [**2**]BAr$^F{}_4$, with the exception of the counteranion.

X-ray Crystallography

X-ray crystallographic and structure refinement details

A colorless block of $[Cu(COD)_2]BAr^F_4$ (0.1 × 0.10 × 0.09 mm), a yellow block of $[\mathbf{1}]_2[B_{12}Cl_{12}]$ (0.12 × 0.12 × 0.10 mm), an orange block of $[\mathbf{2}]_2[B_{12}Cl_{12}]$ (0.12 × 0.12 × 0.12 mm), a red block of $\mathbf{1}^{red}$ (0.1 × 0.10 × 0.09 mm), and a red block of $\mathbf{2}^{red}$ (0.1 × 0.10 × 0.09 mm) were mounted on a 100 μm MiTeGen microloop and placed on a Bruker PHOTON-III CMOS diffractometer for data collection at 100(2) K ($[\mathbf{1}]_2[B_{12}Cl_{12}]$, $[\mathbf{2}]_2[B_{12}Cl_{12}]$, $\mathbf{1}^{red}$, and $\mathbf{2}^{red}$) or 125(2) K ($[Cu(COD)_2]BAr^F_4$ and $[\mathbf{Cu(LH_3)}]BAr^F_4$). The data collection was carried out using Mo Kα radiation with normal parabolic mirrors. The data intensities were corrected for absorption and decay with SADABS.[9] Final cell constants were obtained from least-squares fits from all reflections. Crystal structure solution was done through intrinsic phasing (SHELXT-2014/5) which provided most non-hydrogen atoms.[10] Full matrix least-squares/difference Fourier cycles were performed (using SHELXL-2018/3 and GUI ShelXle)[11-13] to locate the remaining non-hydrogen atoms. All non-hydrogen atoms were refined with anisotropic displacement parameters. Hydrogen atoms were placed in ideal positions and refined as riding atoms with relative isotropic displacement parameters. Covalent radii calculations were performed with data tabulated by Alvarez et al.[14]

The crystal structures of $[\mathbf{1}]_2[B_{12}Cl_{12}]$ and $[\mathbf{2}]_2[B_{12}Cl_{12}]$ revealed highly a disordered THF molecules on a –3 center. All attempts to model this solvent were unsuccessful. Thus, the SQUEEZE function of the PLATON program was used to remove these solvent molecules from the void space and is described in the CIF.[13] $[Cu(COD)_2]BAr^F_4$ was found to have rotational disorder on several CF_3 groups and was modeled accordingly. The structures of $\mathbf{1}^{red}$ and $\mathbf{2}^{red}$ crystallized with molecules of diethyl ether ($\mathbf{1}^{red}$) and toluene ($\mathbf{2}^{red}$) on crystallographic inversion centers and were modelled with 0.5 occupancies. Further refinement details can be found in the CIF file. Images were rendered using POV–ray.[15] The structures of $[Cu(COD)_2][BAr^F_4]$, $[\mathbf{Cu(LH_3)}]BAr^F_4$), $[\mathbf{1}]_2[B_{12}Cl_{12}]$, $[\mathbf{2}]_2[B_{12}Cl_{12}]$, $\mathbf{1}^{red}$, and $\mathbf{2}^{red}$ were deposited in the Cambridge Crystallographic Data Centre structural database (CCDC 2076274–2076278 and 2092926).

Table S1. Crystallographic details for $[Cu(COD)_2]BAr^F_4$, $[\mathbf{1}]_2[B_{12}Cl_{12}]$, $[\mathbf{2}]_2[B_{12}Cl_{12}]$, $\mathbf{1}^{red}$, $\mathbf{2}^{red}$, and $[\mathbf{Cu(LH_3)}]BAr^F_4$. *Note: Cations $[\mathbf{1}]^+$ and $[\mathbf{2}]^+$ are characterized crystallographically as $[B_{12}Cl_{12}]^{2-}$ salts.

Complex	$[Cu(COD)_2]$ BAr^F_4	$[\mathbf{1}]_2[B_{12}Cl_{12}]$	$[\mathbf{2}]_2[B_{12}Cl_{12}]$	$\mathbf{1}^{red}$	$\mathbf{2}^{red}$	$[\mathbf{Cu(LH_3)}]$ BAr^F_4
chemical formula	$[C_{16}H_{24}Cu]$ $C_{32}H_{12}BF_{24}$	$[C_{39}H_{60}N_4P_3AlCu]_2$ $B_{12}Cl_{12}$	$[C_{39}H_{60}N_4P_3GaCu]_2$ $B_{12}Cl_{12}$	$C_{39}H_{60}N_4P_3AlCu$ $\cdot 0.5(C_4H_{10}O)$	$C_{39}H_{60}N_4P_3GaCu$ $\cdot 0.5(C_7H_8)$	$[C_{39}H_{63}N_4P_3Cu]$ $C_{32}H_{12}BF_{24}$
CCDC No.	2076274	2076275	2076276	2076277	2076278	2092926
Fw	1143.22	2091.82	2177.39	805.40	857.14	1607.61
cryst syst	orthorhombic	trigonal	trigonal	triclinic	triclinic	monoclinic
space group	Pbca	$P\bar{3}c1$	$P\bar{3}c1$	$P\bar{1}$	$P\bar{1}$	$P2_1/n$
a (Å)	18.0783(8)	14.9086(7)	14.9147(15)	11.2148(7)	11.344(4)	14.9684(6)
b (Å)	19.0664(8)	14.9086(7)	14.9147(15)	14.0921(10)	14.194(4)	25.1887(9)
c (Å)	27.2154(11)	26.6016(14)	26.629(3)	14.3396(9)	14.285(5)	19.9836(7)
α (deg)	90	90	90	70.906(2)	70.274(17)	90
β (deg)	90	90	90	82.680(2)	79.551(17)	95.9370(10)
γ (deg)	90	120	120	80.584(2)	82.067(14)	90
V (Å^3)	9380.8(7)	5120.5(6)	5129.9(12)	2106.0(2)	2122.0(12)	7494.1(5)
Z	8	2	2	2	2	4
D_{calcd} (g cm^{-3})	1.619	1.436	1.410	1.270	1.342	1.425
λ (Å), μ (mm^{-1})	0.71073, 0.597	0.71073, 0.889	0.71073, 1.379	0.71073, 0.688	0.7107, 1.283	0.7107, 0.459
T (K)	125(2)	100(2)	100(2)	100(2)	100(2)	125(2)
θ range (deg)	2.136–27.209	2.198–36.342	2.197–36.309	2.472-–3.194	2.294–36.427	2.118–31.556
reflns collected	10399	52877	88036	36969	57673	25005
unique reflns	6965	8281	8281	15939	20377	19412
data/restraints/param	6965/83/727	8281/0/185	8281/0/185	15939/3/492	20377/74/493	19412/51/991
R_1, wR_2 ($I > 2\sigma(I)$)	0.0682, 0.2119	0.0412, 0.1101	0.0434, 0.1277	0.0332, 0.0842	0.0286, 0.0728	0.0434, 0.1078
R_1, wR_2 (all data)	0.1053, 0.2119	0.0543, 0.1170	0.0545, 0.1368	0.0460, 0.0898	0.0365, 0.0773	0.0640, 0.1230

Table S2. Geometrical Parameters including bond lengths (Å) and angles (°) for, $[\mathbf{1}]_2[B_{12}Cl_{12}]$, $[\mathbf{2}]_2[B_{12}Cl_{12}]$, $\mathbf{1}^{red}$, $\mathbf{2}^{red}$, and $[\mathbf{Cu(LH_3)}]BAr^F{}_4$. *Note: Cations $[\mathbf{1}]^+$ and $[\mathbf{2}]^+$ are characterized crystallographically as $[B_{12}Cl_{12}]^{2-}$ salts.

Parameter (Å or °)	$[\mathbf{1}]_2[B_{12}Cl_{12}]$	$\mathbf{1}^{red}$	$[\mathbf{2}]_2[B_{12}Cl_{12}]$	$\mathbf{2}^{red}$	$[Cu(LH_3)]BAr^F{}_4$
M–Cu	2.6239(8)	2.5298(4)	2.5737(5)	2.4541(6)	–
r^a	1.04	1.00	1.01	0.97	–
Cu–P^b	2.2925(4)	2.2476(4)	2.2994(5)	2.2689(7)	2.2971(4)
	–	2.2477(4)	–	2.2693(7)	2.3010(4)
	–	2.2508(3)	–	2.2712(7)	2.3022(4)
M–N_{eq}	1.8546(12)	1.8882(10)1.89	1.9059(14)	1.9549(9)	–
	–	06(10)	–	1.9549(9)	
	–	1.8957(10)	–	1.9624(10)	
M–N_{ap}	2.000(2)	2.0836(10)	2.069(3)	2.1948(9)	–
Cu to P3-plane	0.188	0.118	0.180	0.136	0.027
M to N3-plane	0.07	0.246	0.142	0.355	–
∑(∡P–Cu–P)	358.02(1)	359.18(2)	358.19(2)	358.93(4)	359.96(5)
∑(∡N_{eq}–M–N_{eq})	359.47(1)	355.01(1)	358.36(2)	350.36(4)	

^{a}Ratio of the M–Cu bond length to the sum of Al/Ga and Cu covalent radii.[14] ^{b}Trigonal space groups only display one value by symmetry.

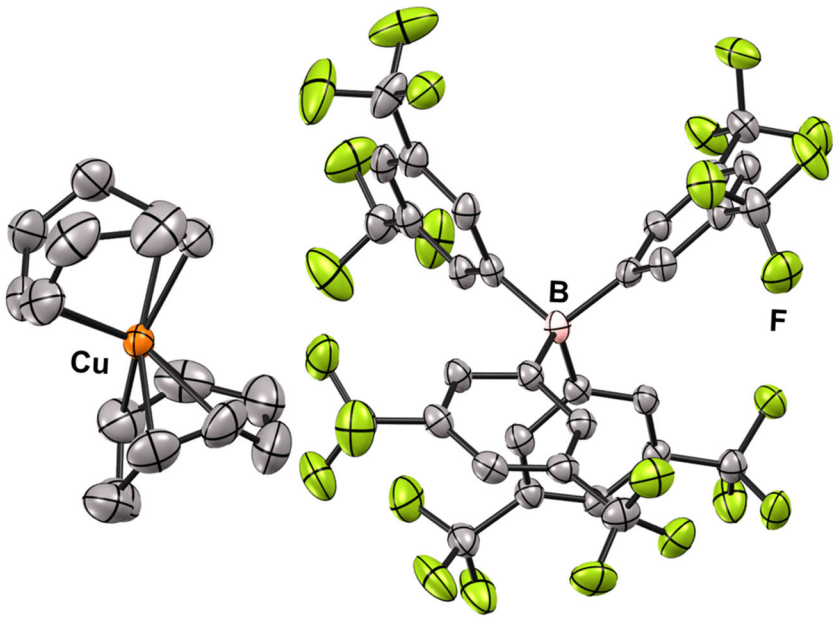

Figure S1. Molecular structure of $[Cu(COD)_2]BAr^F{}_4$ shown at 50% thermal ellipsoid probability.

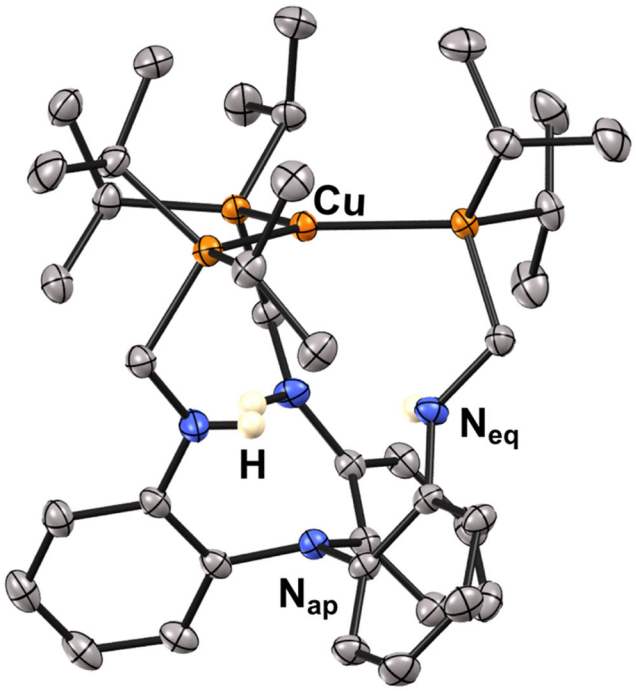

Figure S2. Molecular structure of $[\mathbf{Cu(LH_3)}]BAr^F{}_4$ shown at 50% thermal ellipsoid probability. All hydrogens are omitted for clarity except N–H. The $BAr^F{}_4^-$ counter anion is omitted.

NMR Spectroscopy of Cu Complexes

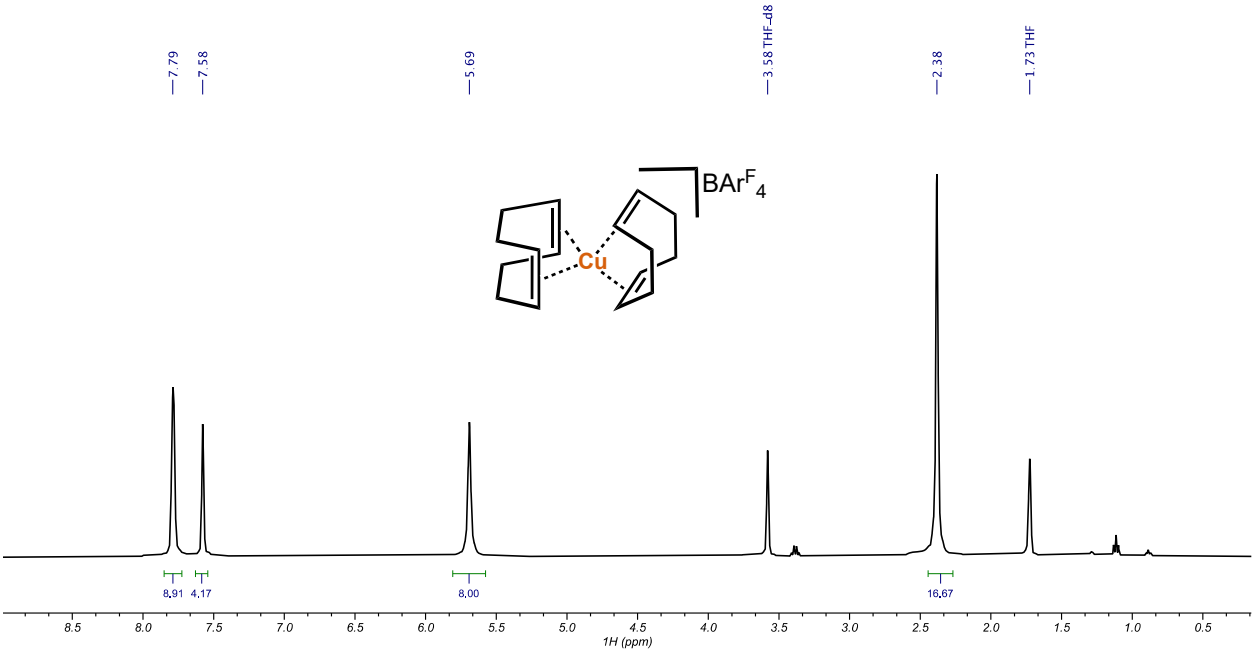

Figure S3. ^{1}H NMR spectrum (400 MHz, THF-d_8) of [Cu(COD)$_2$]BAr$^F_4$.

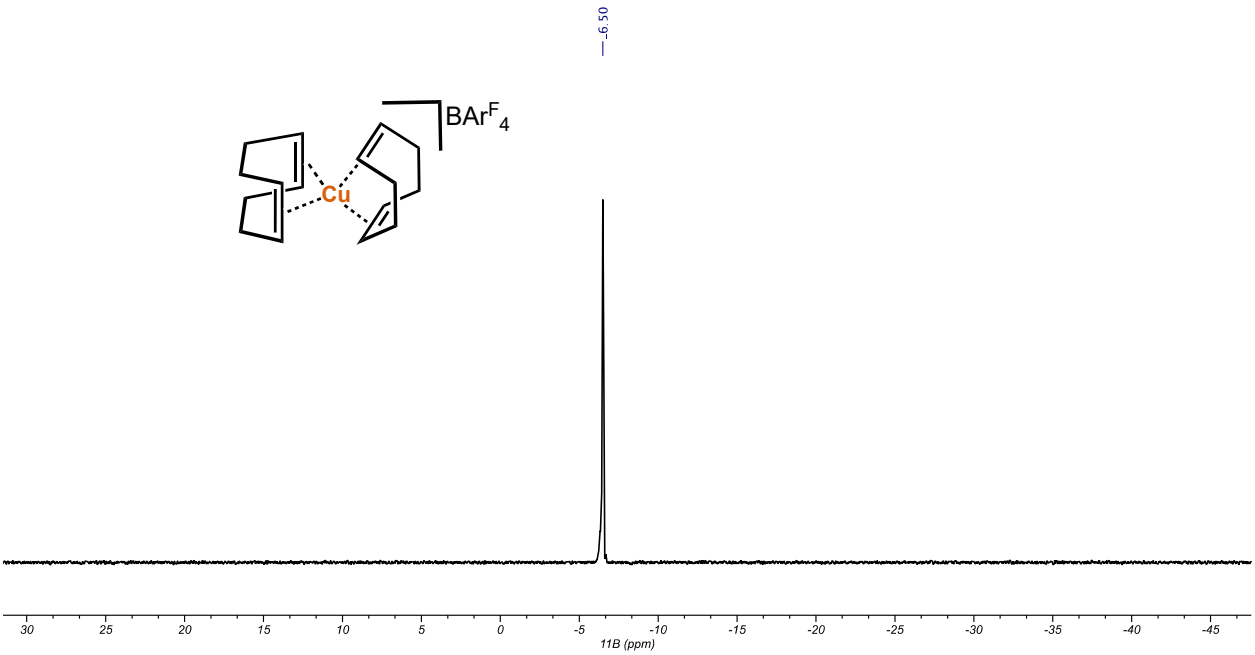

Figure S4. ^{11}B NMR spectrum (128 MHz, THF-d_8) of **[**Cu(COD)$_2$**]**BAr$^F_4$.

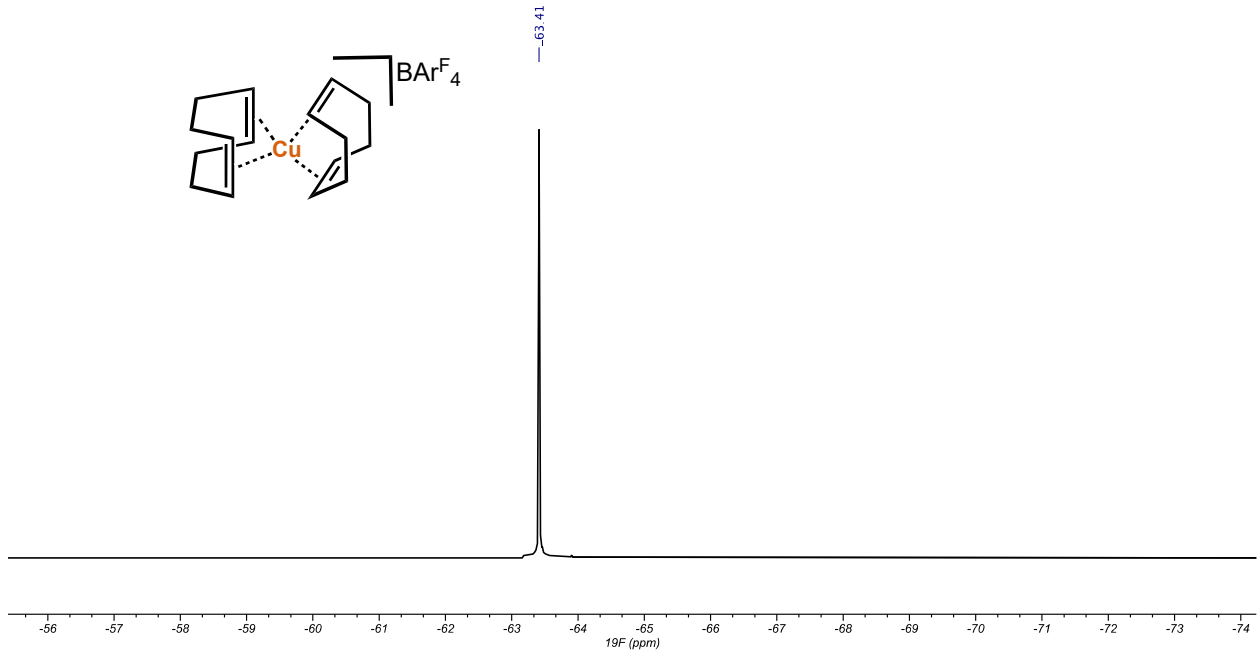

Figure S5. $^{19}F\{^1H\}$ NMR spectrum (376 MHz, THF-d_8) of $[Cu(COD)_2]BAr^F_4$.

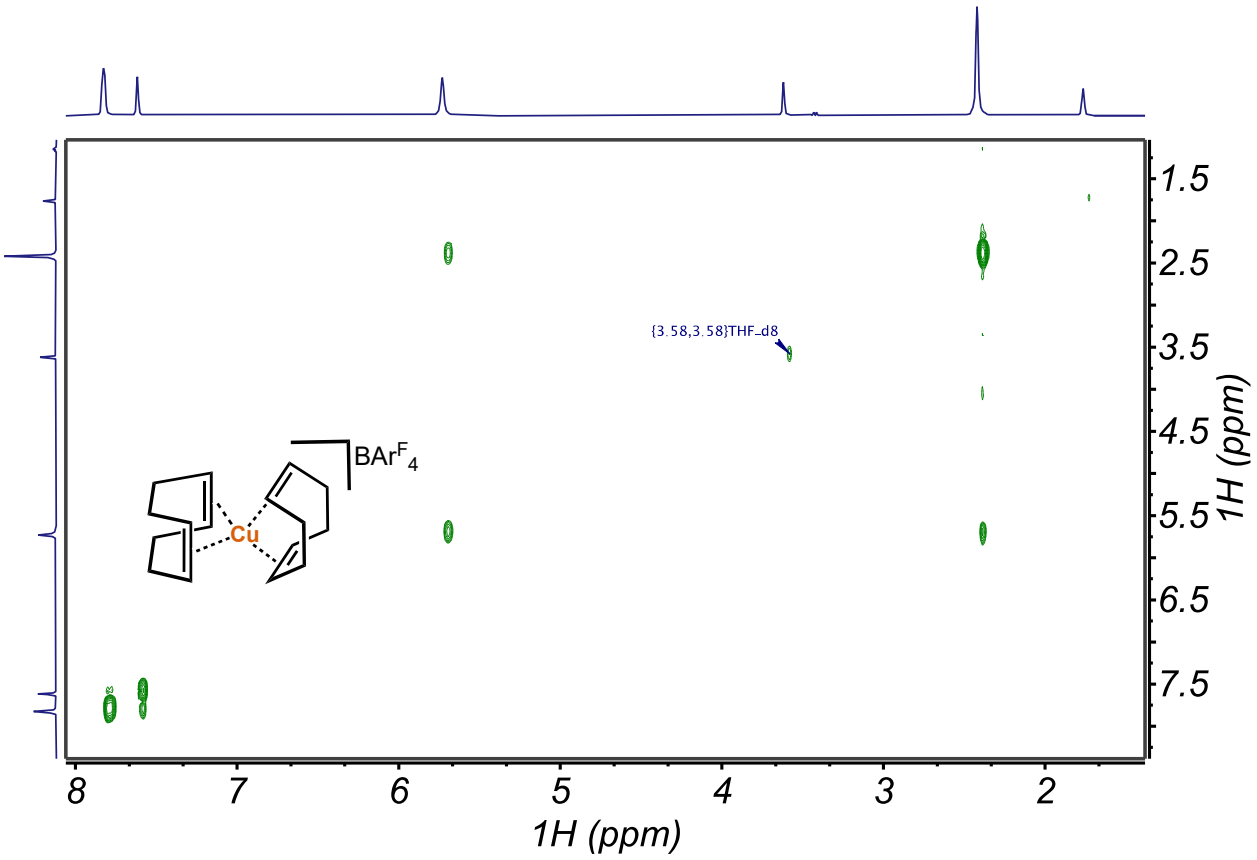

Figure S6. ^1H–^1H COSY NMR spectrum in THF-d_8 of $[Cu(COD)_2]BAr^F_4$.

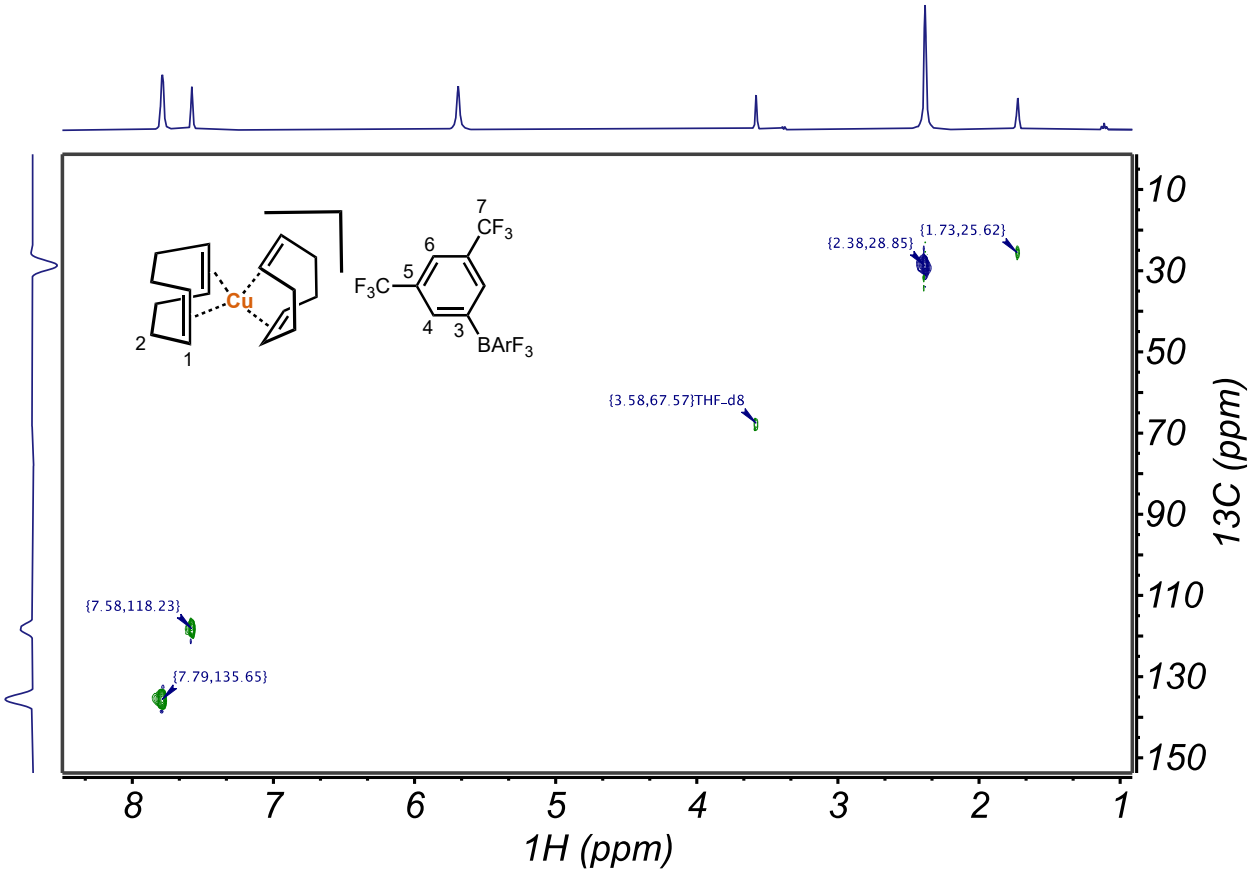

Figure S7. $^{1}H–^{13}C$ HSQC NMR spectrum in THF-d_8 of $[Cu(COD)_2]BAr^F{}_4$.

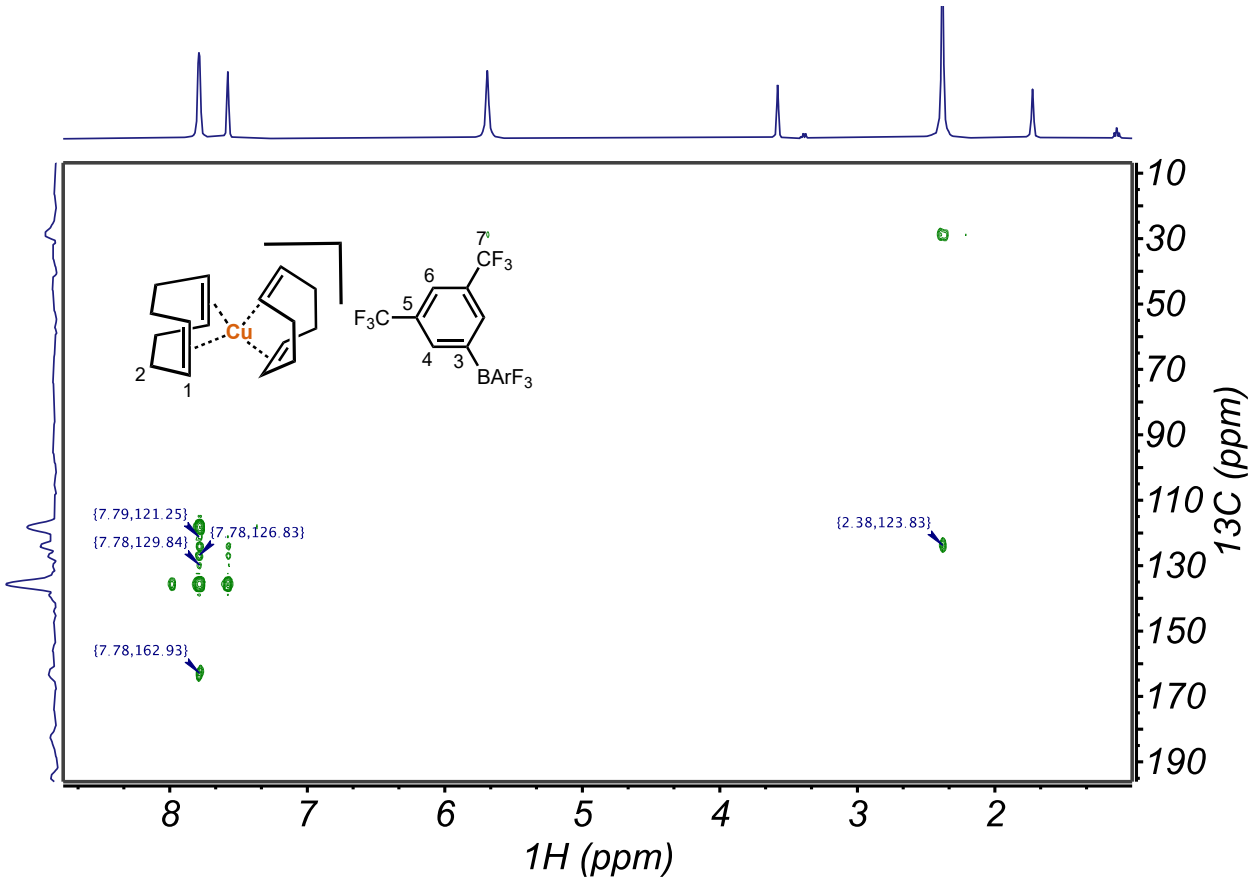

Figure S8. $^{1}H–^{13}C$ HMBC NMR spectrum in THF-d_8 of $[Cu(COD)_2]BAr^F{}_4$.

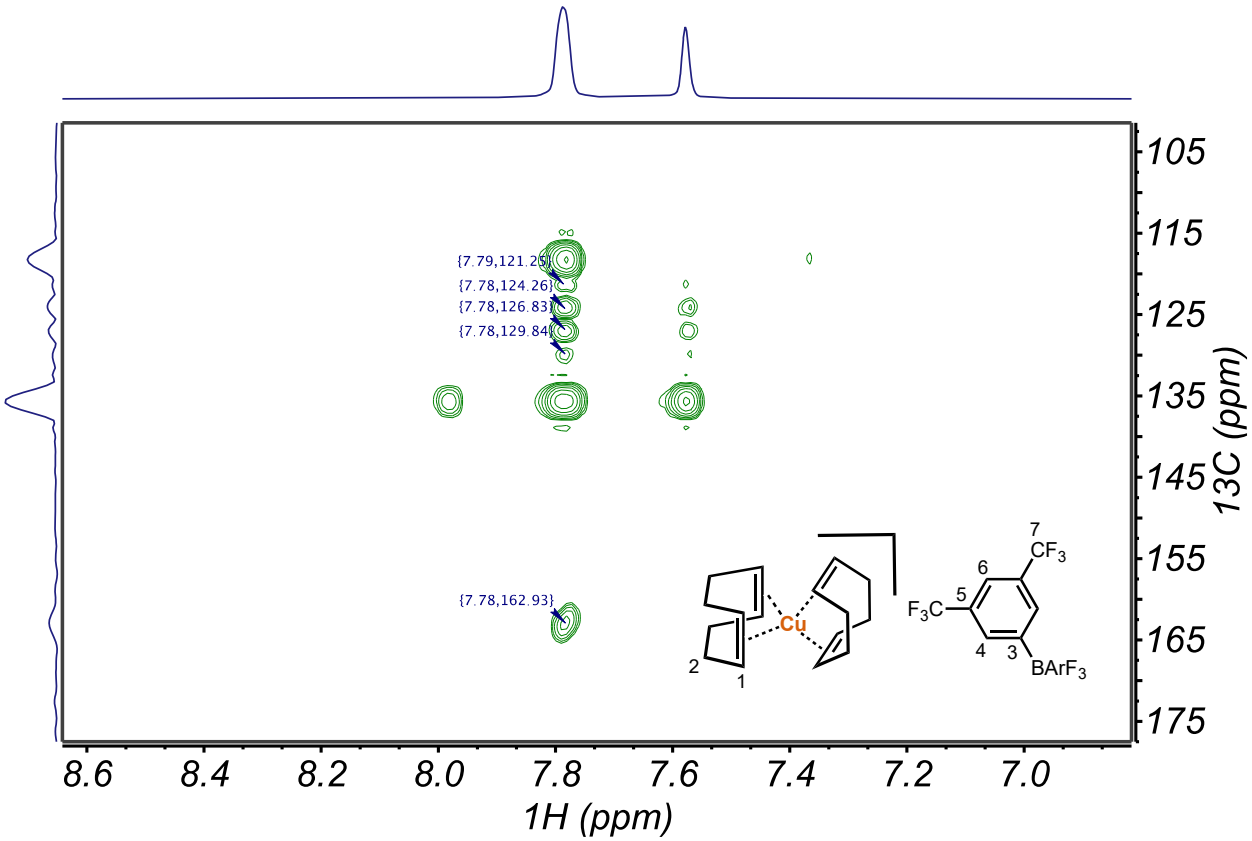

Figure S9. Zoom of aryl region in $^{1}H–^{13}C$ HMBC NMR spectrum in THF-d_8 of $[Cu(COD)_2]BAr^{F}_4$.

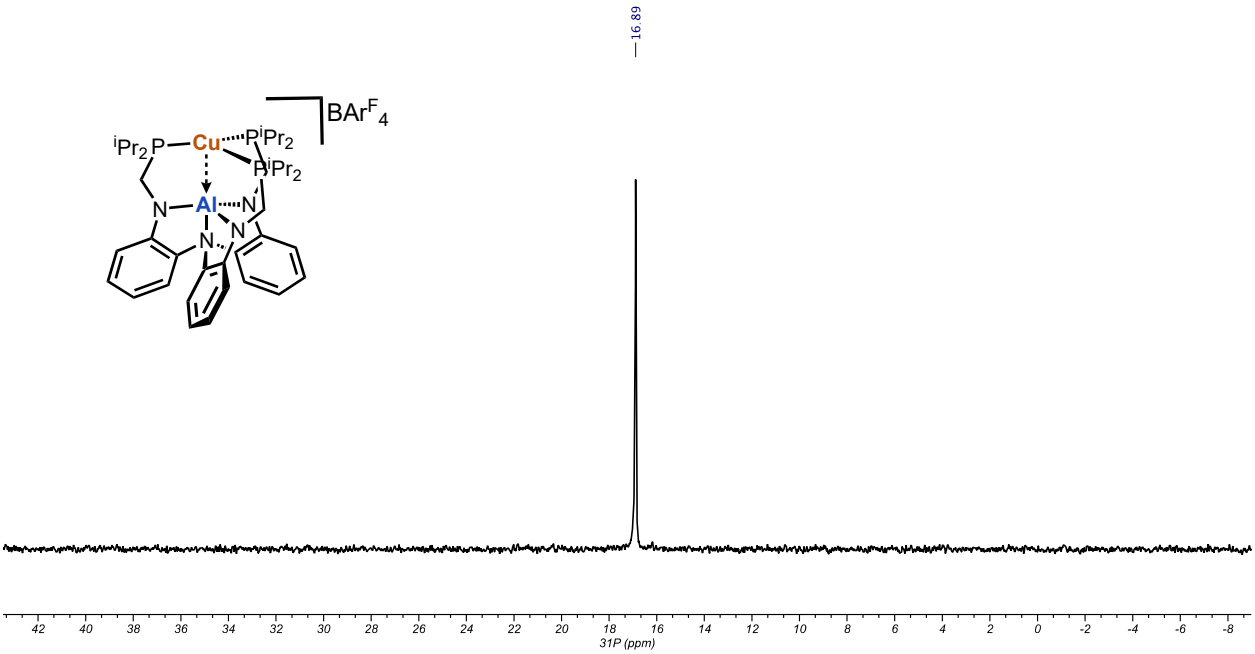

Figure S10. $^{31}P\{^1H\}$ NMR spectrum (162 MHz, C_6D_6) of [**1**]BAr^F_4.

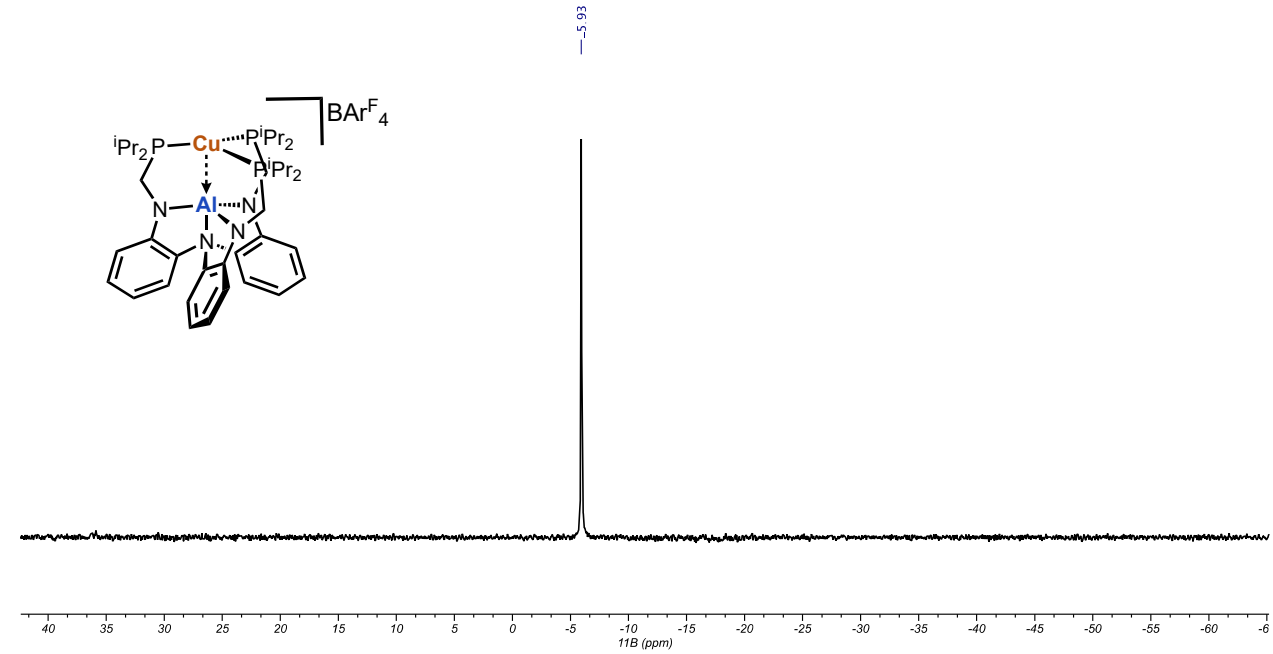

Figure S11. ^{11}B NMR spectrum (128 MHz, C_6D_6) of [**1**]BAr^F_4.

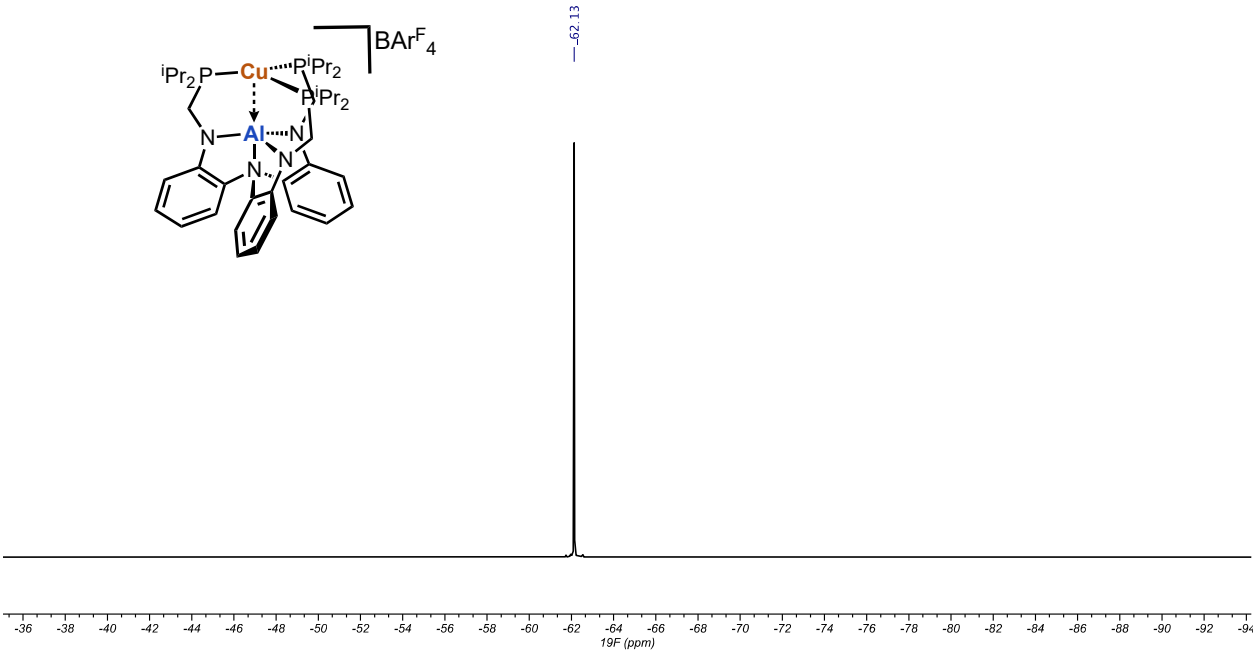

Figure S12. $^{19}F\{^1H\}$ NMR spectrum (376 MHz, C_6D_6) of [**1**]BAr$^F_4$.

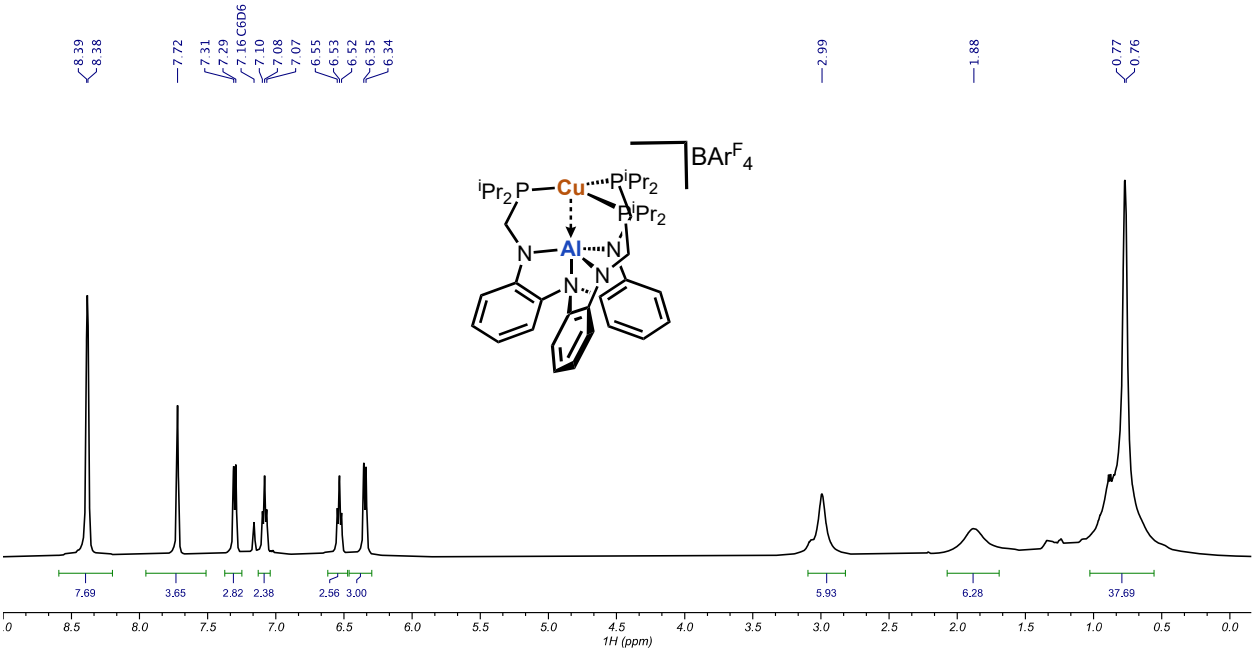

Figure S13. ^1H NMR spectrum (400 MHz, C_6D_6) of [**1**]BAr$^F_4$.

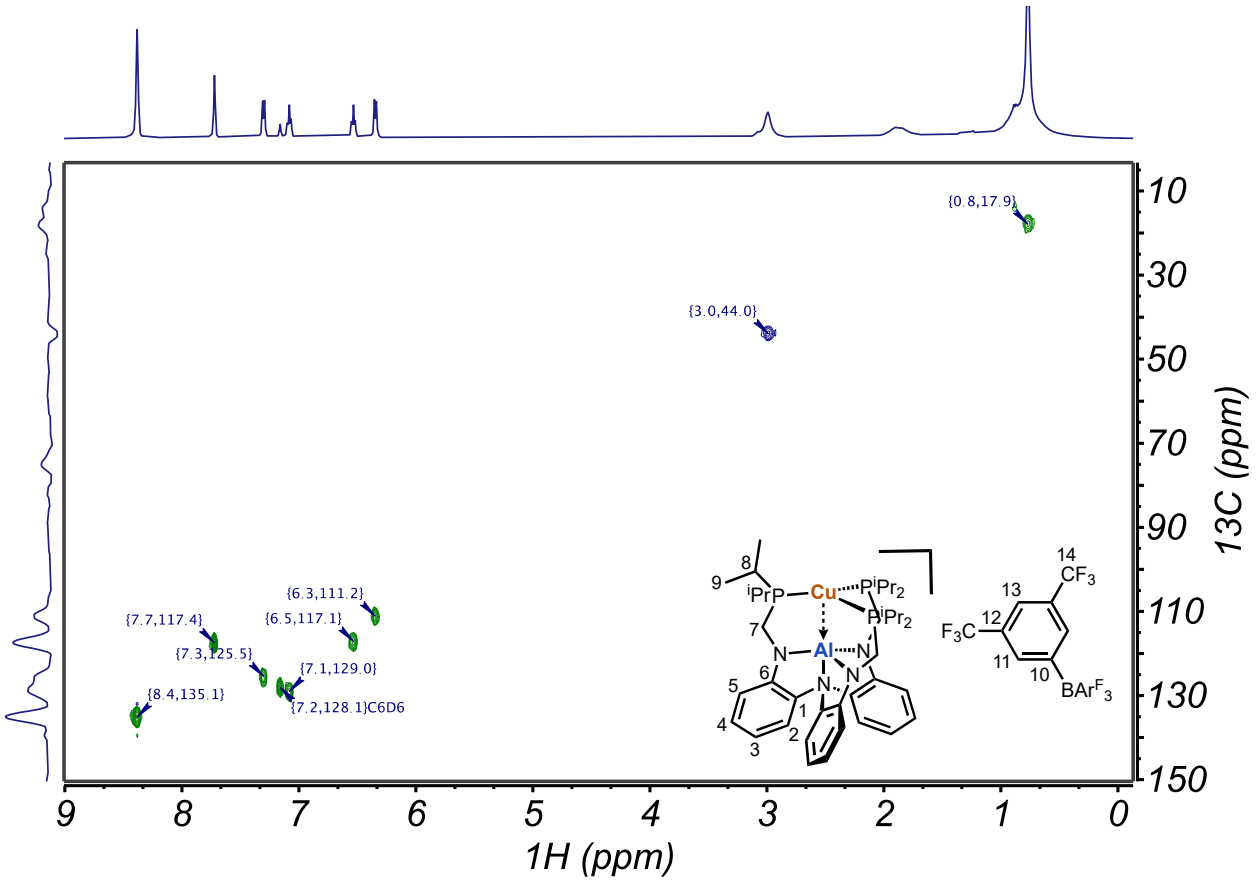

Figure S14. $^{1}H–^{13}C$ HSQC NMR spectrum in C_6D_6 of [**1**]BAr^{F}_4.

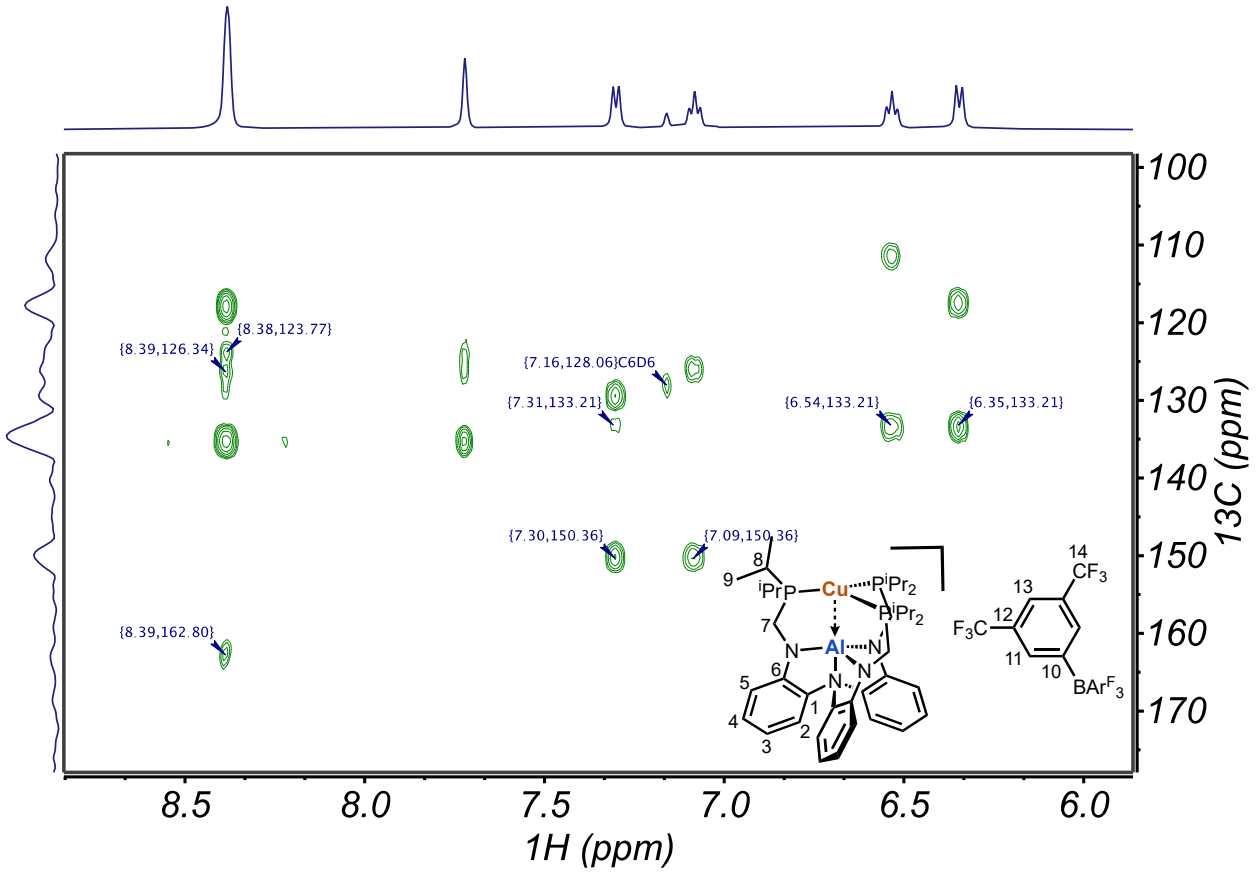

Figure S15. Zoom of $^{1}H–^{13}C$ HMBC NMR spectrum in C_6D_6 of [**1**]BAr^{F}_4.

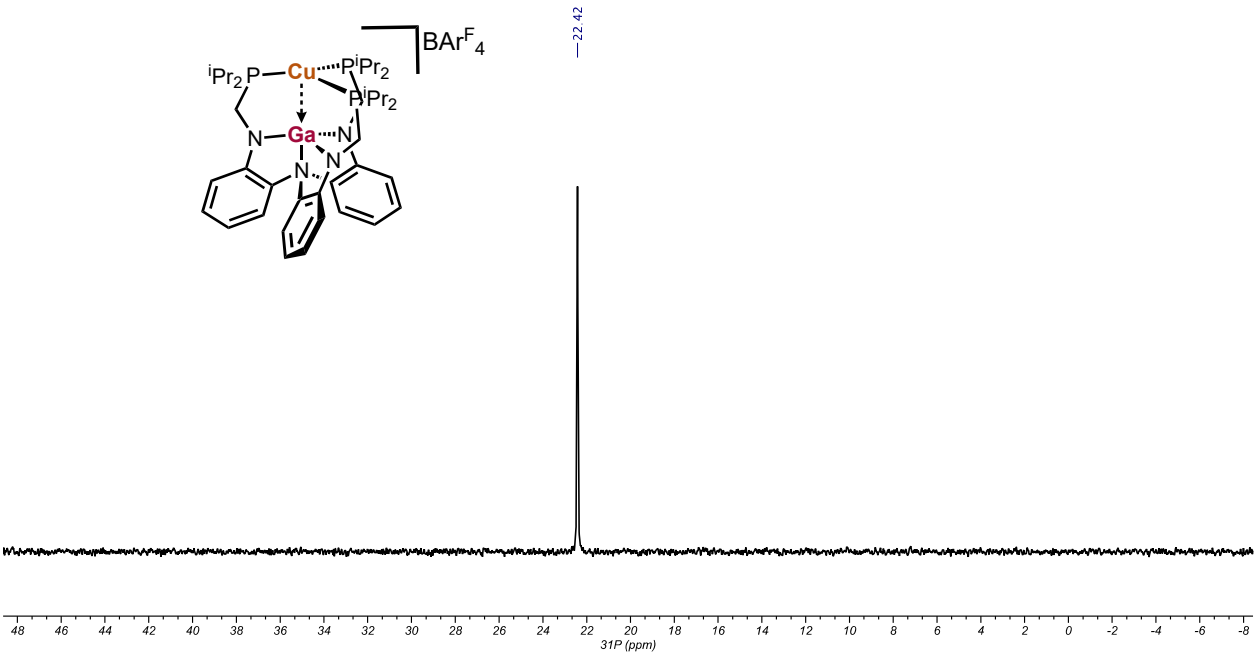

Figure S16. $^{31}P\{^1H\}$ NMR spectrum (162 MHz, C_6D_6) of [**2**]BAr$^F_4$.

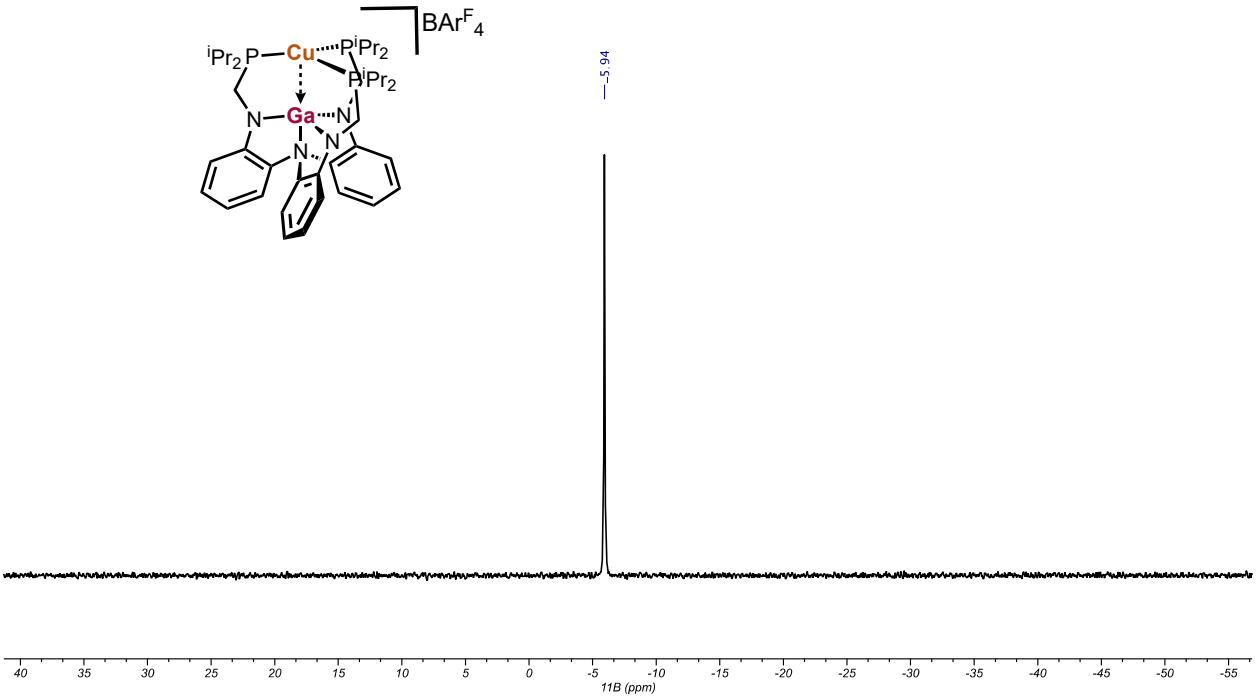

Figure S17. ^{11}B NMR spectrum (128 MHz, C_6D_6) of [**2**]BAr$^F_4$.

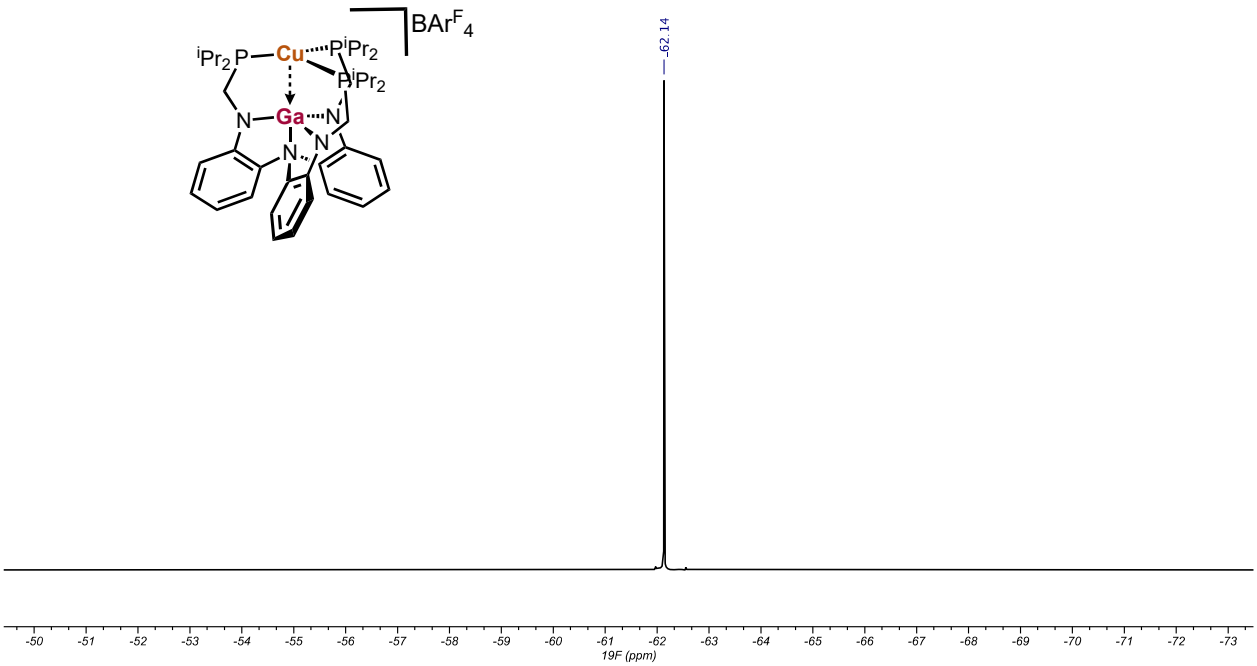

Figure S18. $^{19}F\{^1H\}$ NMR spectrum (376 MHz, C_6D_6) of [**2**]BAr$^F_4$.

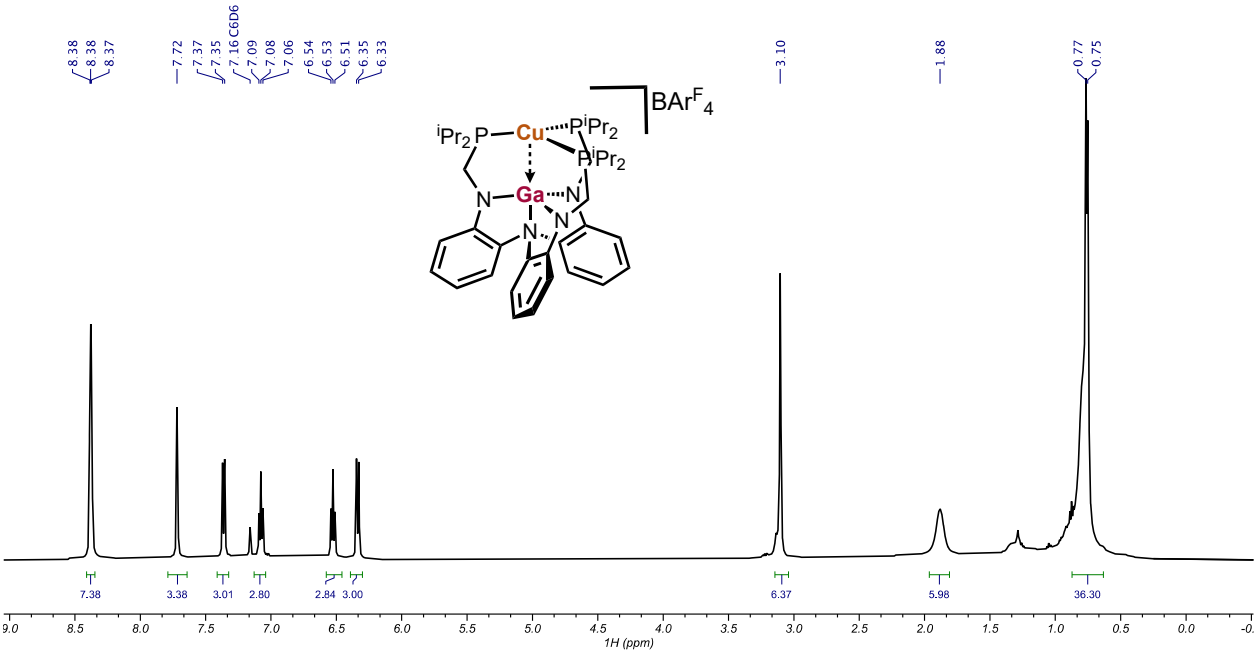

Figure S19. ^1H NMR spectrum (400 MHz, C_6D_6) of [**2**]BAr$^F_4$.

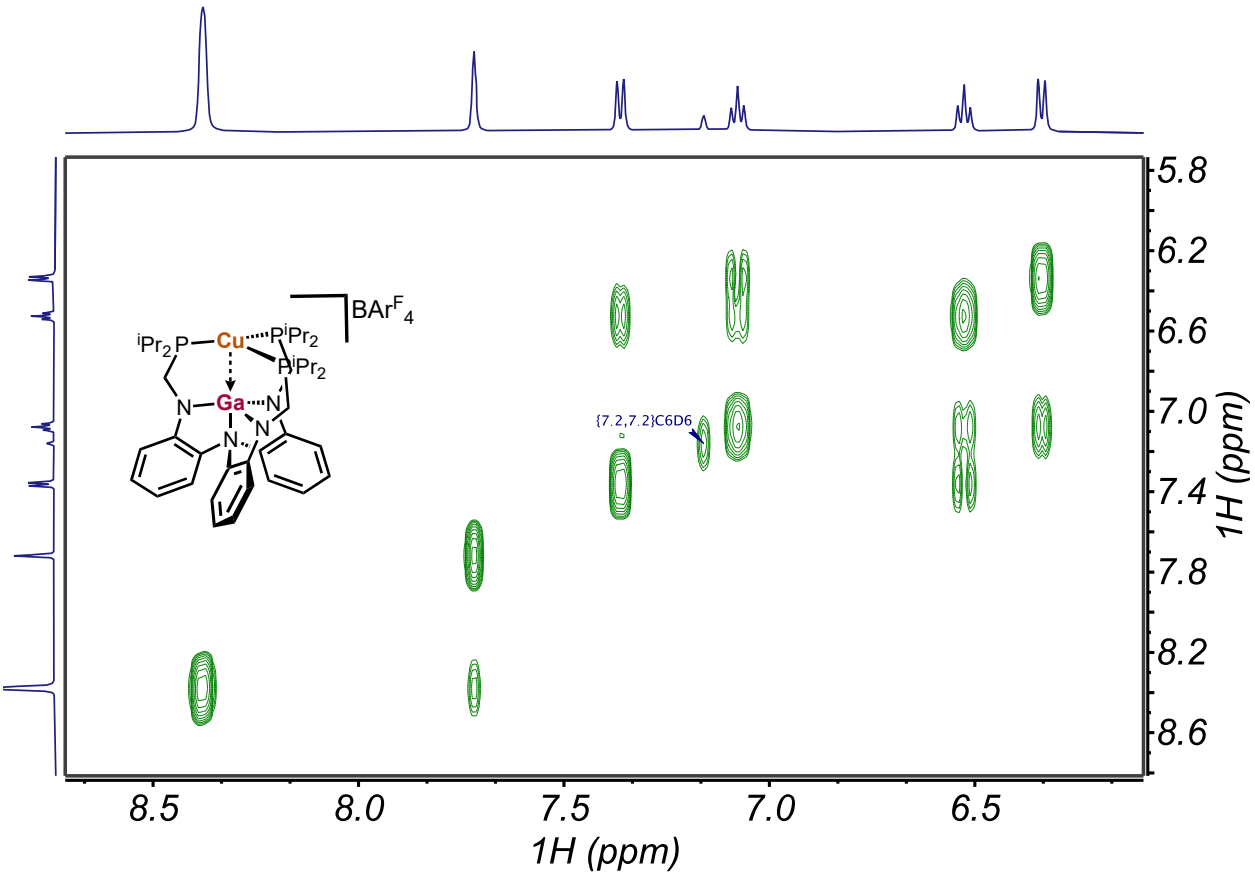

Figure S20. Zoom of aryl region in ^{1}H–^{1}H COSY NMR spectrum in C_6D_6 of [**2**]BAr$^F_4$.

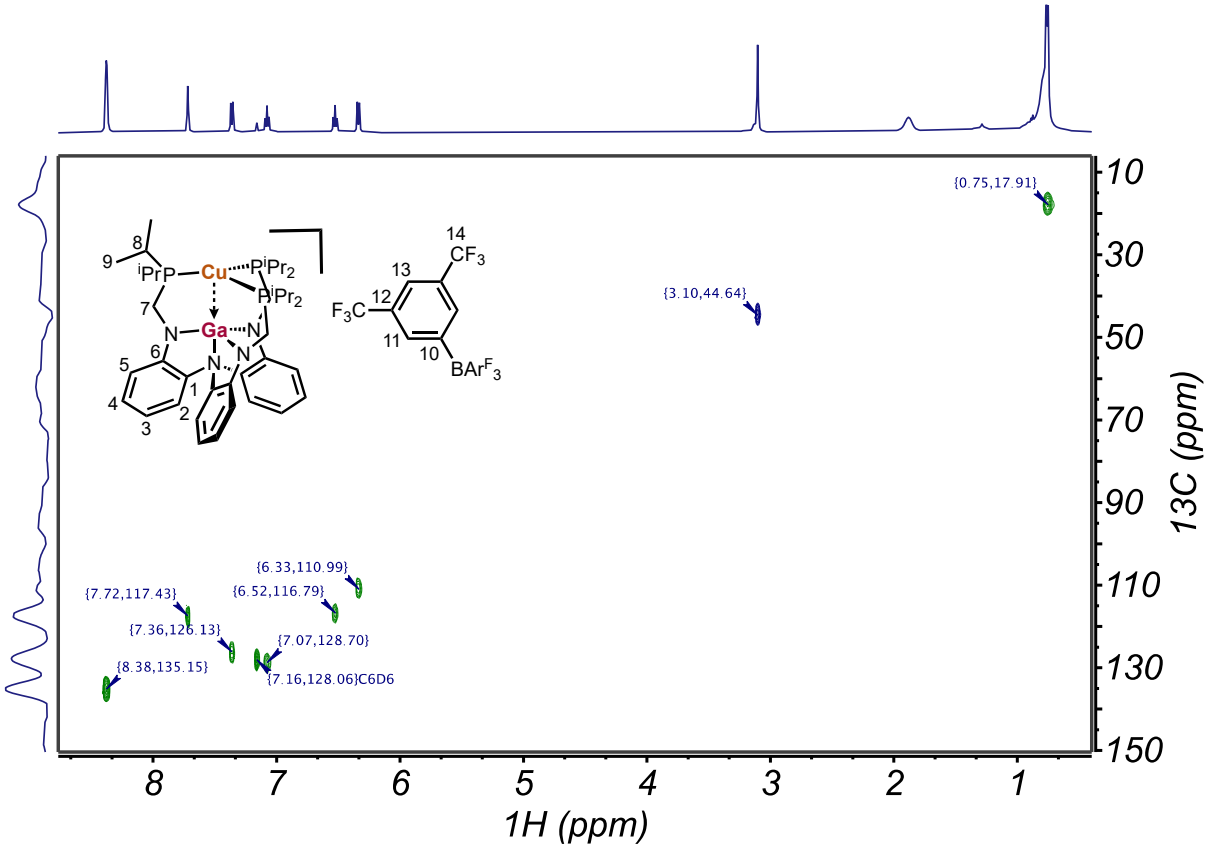

Figure S21. ^{1}H–^{13}C HSQC NMR spectrum in C_6D_6 of [**2**]BAr$^F_4$.

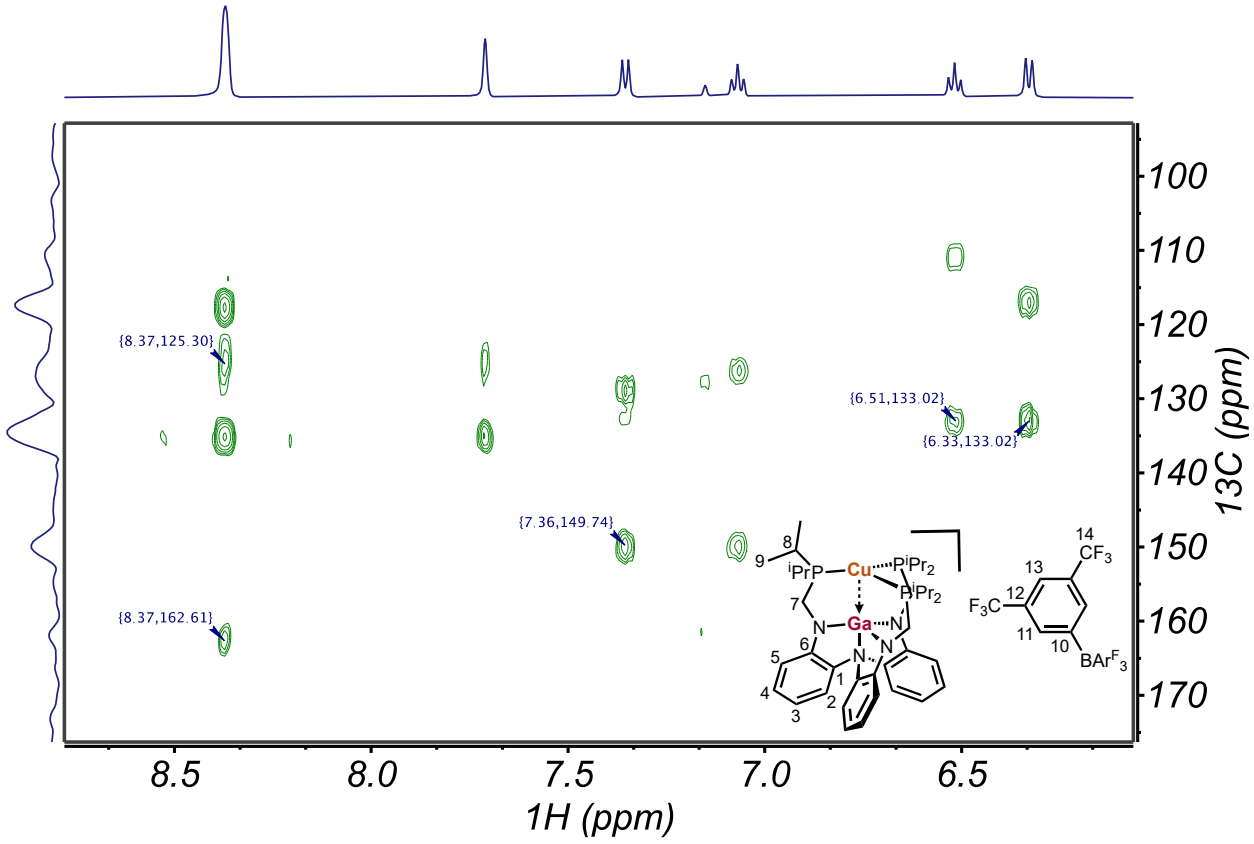

Figure S22. Zoom of aryl region in ^{1}H–^{13}C HMBC NMR spectrum in C_6D_6 of [**2**]BAr^F_4.

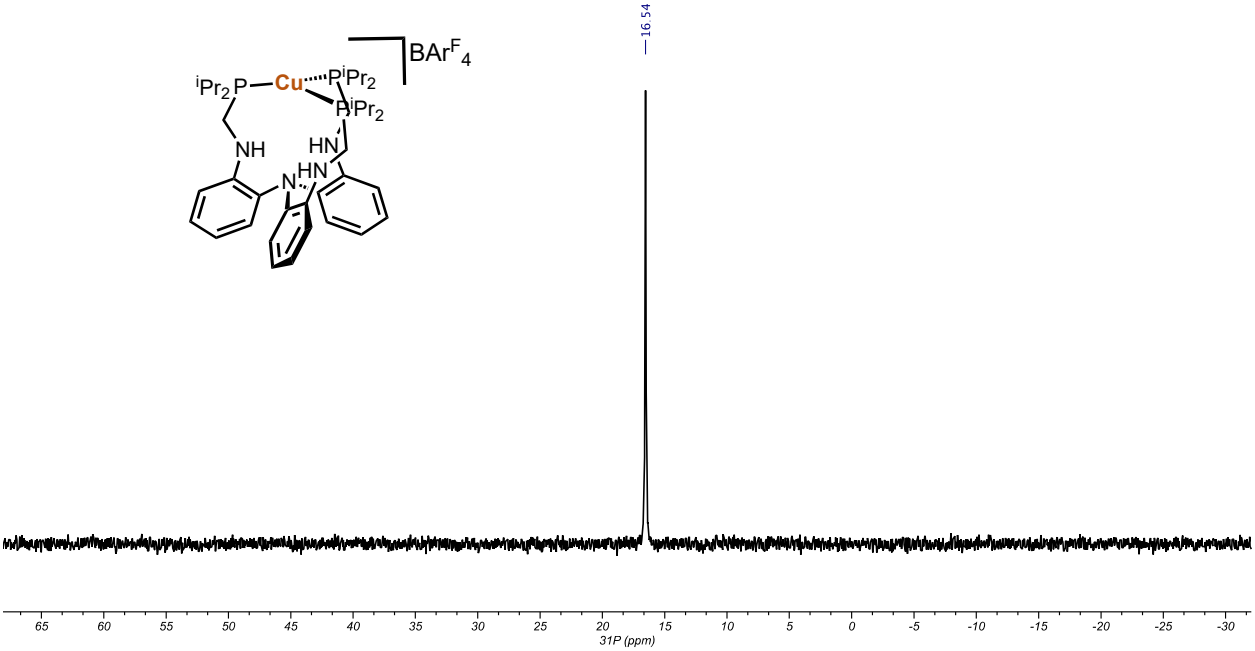

Figure S23. $^{31}P\{^{1}H\}$ NMR spectrum (162 MHz, C_6D_6) of [**Cu(LH$_3$)**]BAr^F_4.

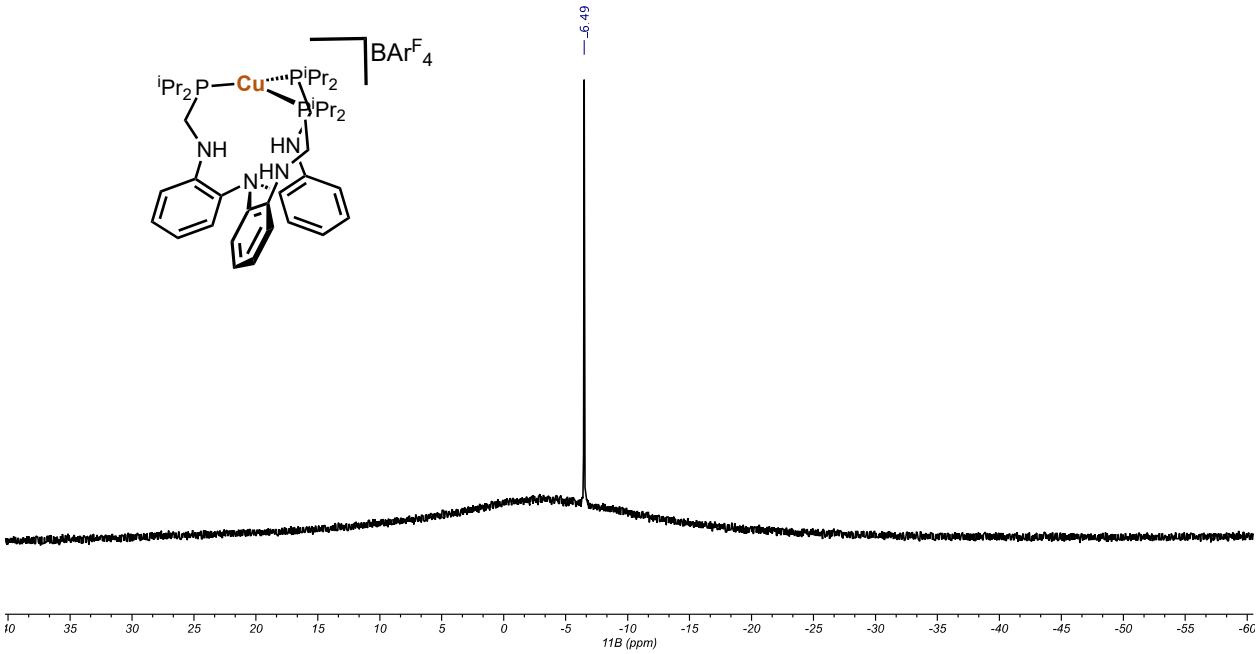

Figure S24. ^{11}B NMR spectrum (128 MHz, THF-d_8) of [**Cu(LH$_3$)**]BAr$^F_4$.

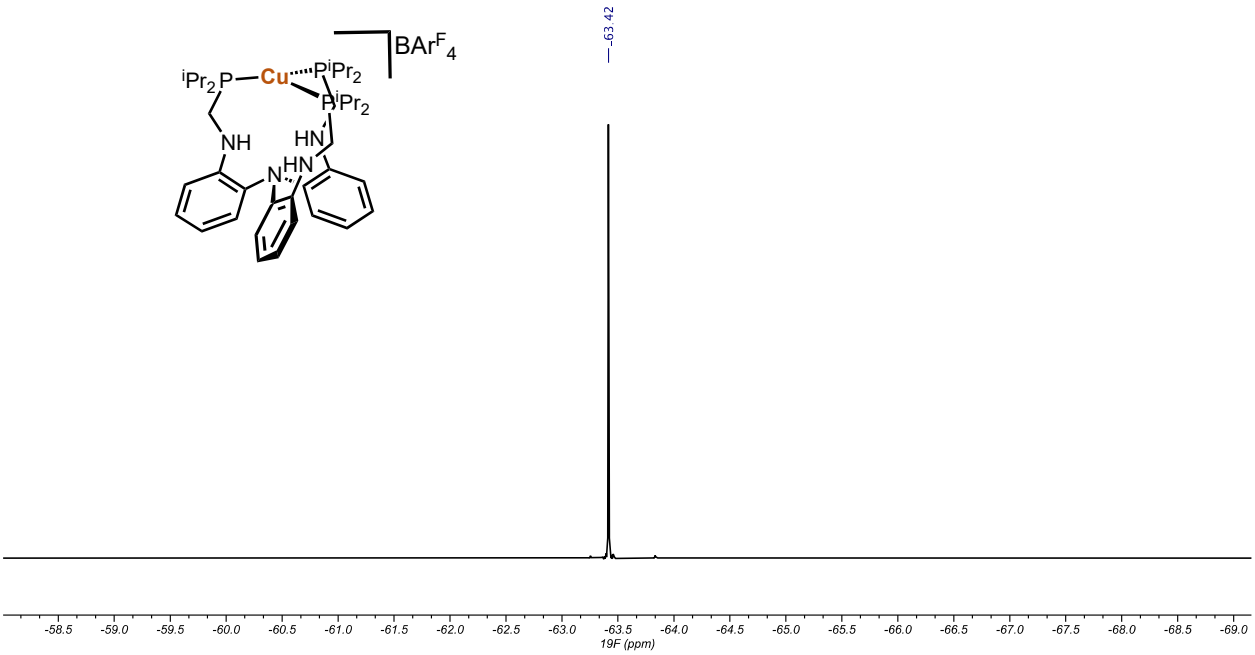

Figure S25. ^{19}F{^{1}H} NMR spectrum (376 MHz, THF-d_8) of [**Cu(LH$_3$)**]BAr$^F_4$**.**

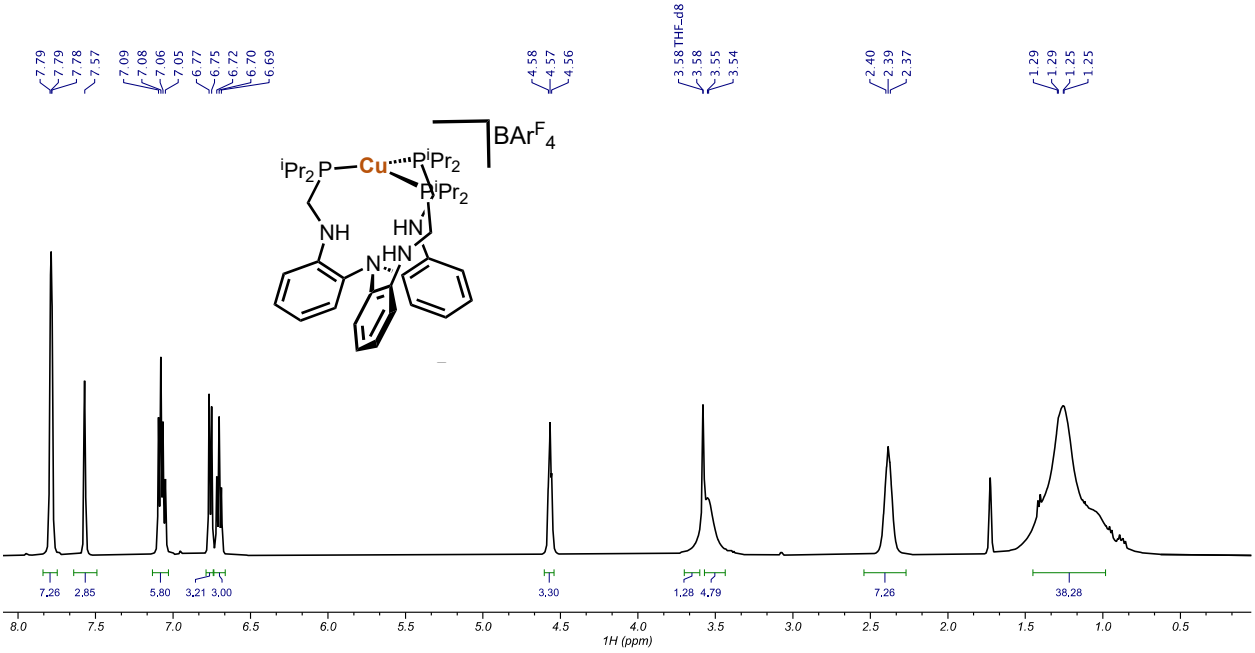

Figure S26. ^{1}H NMR spectrum (400 MHz, THF-d_8) of [**Cu(LH$_3$)**]BAr$^F_4$.

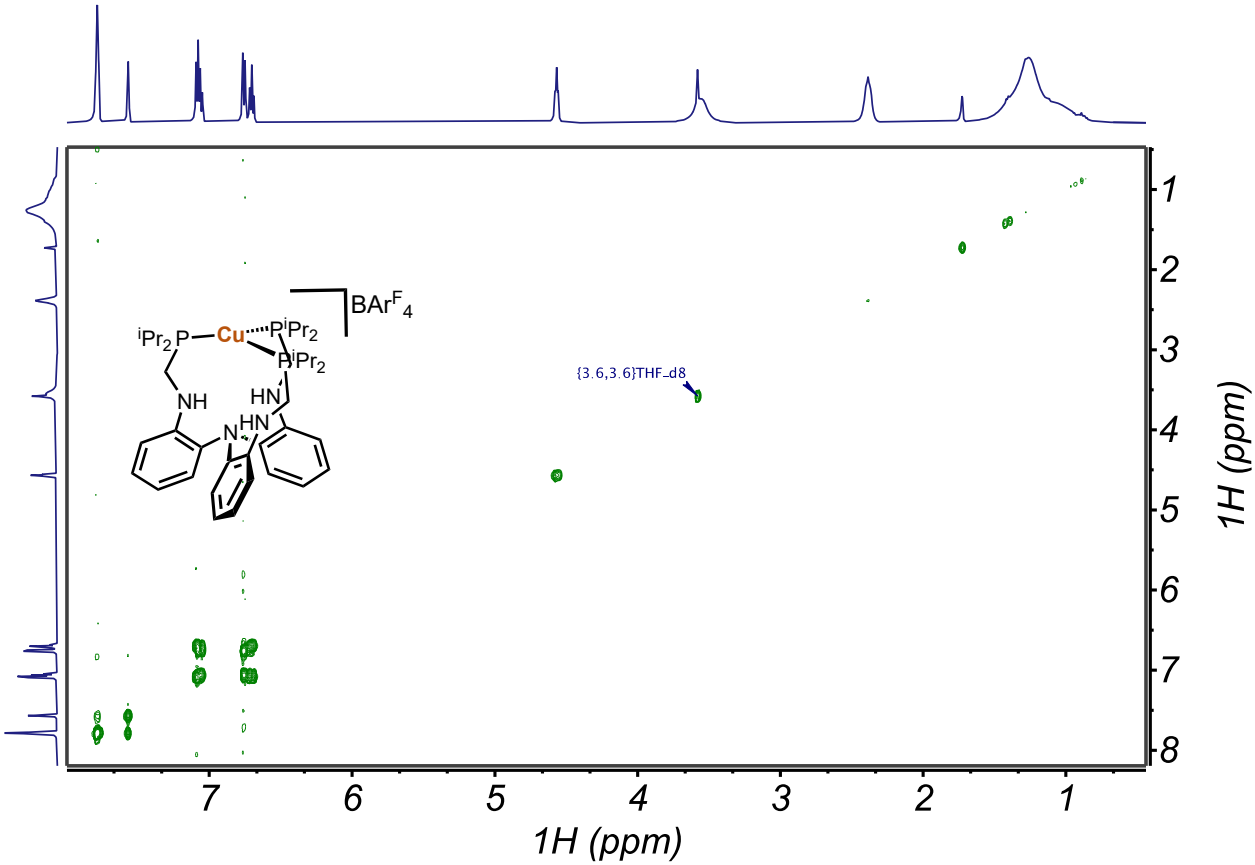

Figure S27. Zoom of aryl region in ^{1}H–^{1}H COSY NMR spectrum in THF-d_8 of [**Cu(LH$_3$)**]BAr$^F_4$.

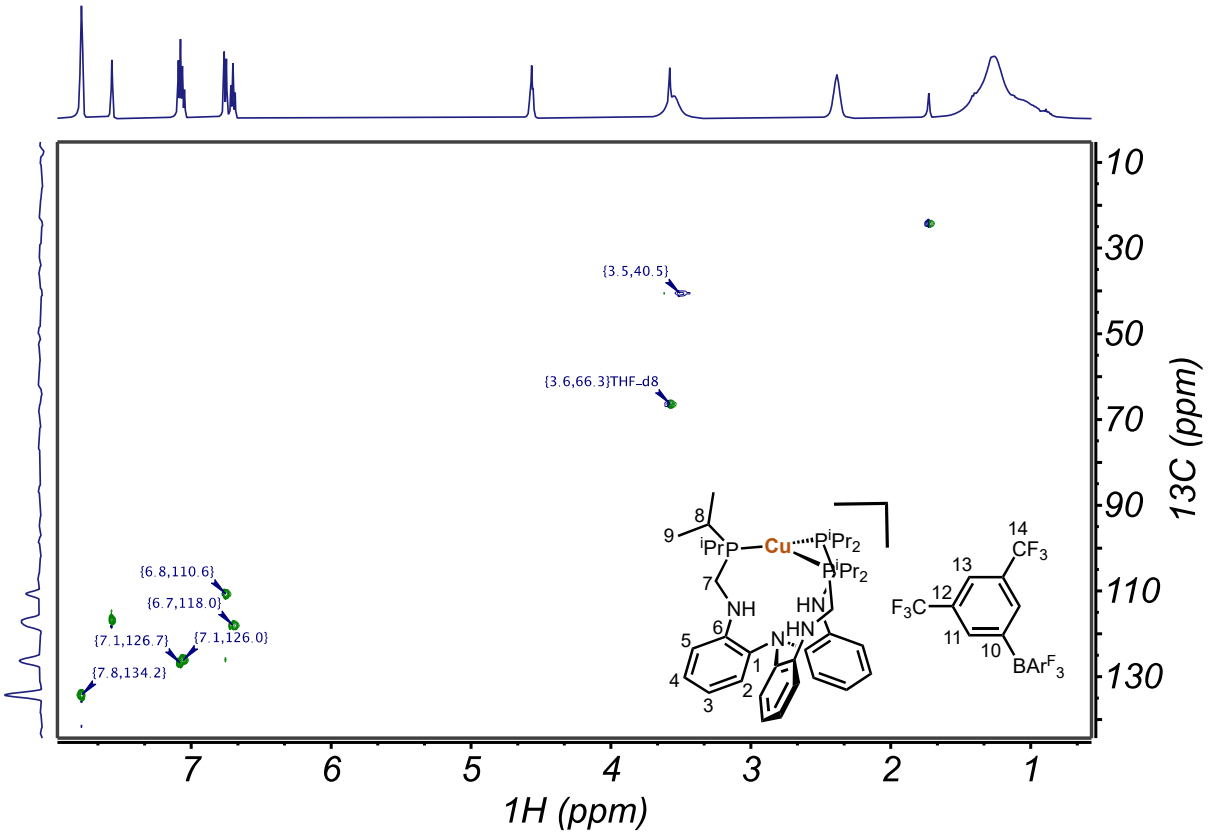

Figure S28. ^{1}H–^{13}C HSQC NMR spectrum in THF-d_8 of [**Cu(LH$_3$)**]BAr$^F_4$.

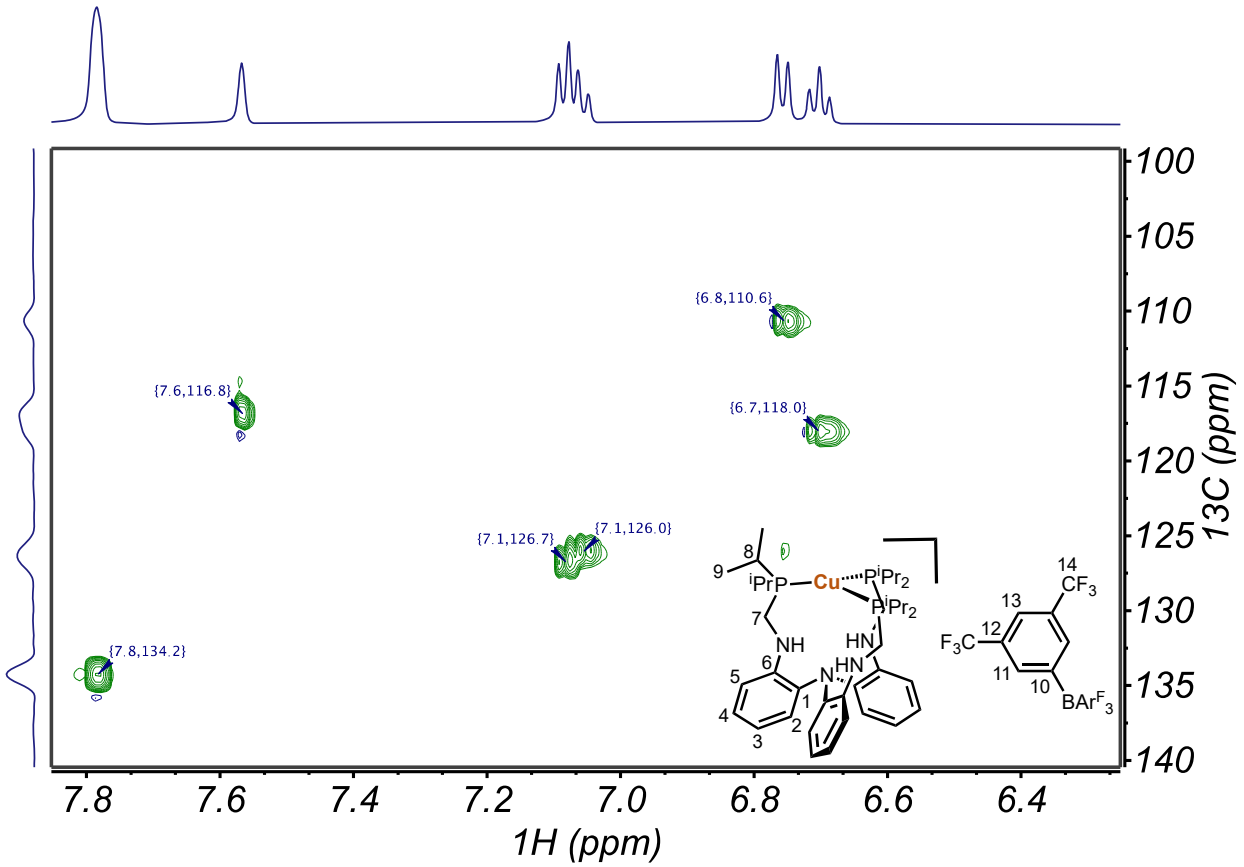

Figure S29. Zoom of ^{1}H–^{13}C HSQC NMR spectrum in THF-d_8 of [**Cu(LH$_3$)**]BAr$^F_4$.

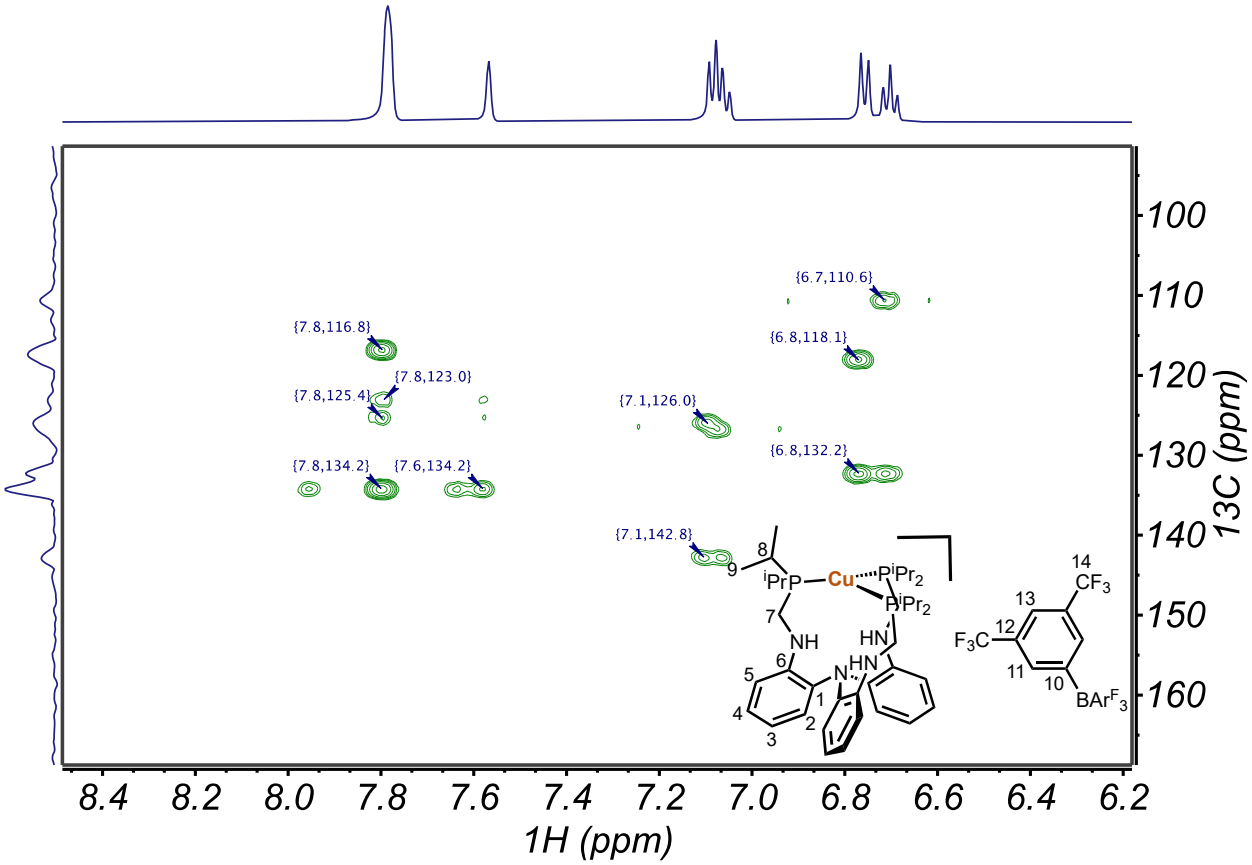

Figure S30. Zoom of ^{1}H–^{13}C HMBC NMR spectrum in THF-d_8 of [**Cu(LH$_3$)**]BAr$^F_4$.

Cyclic Voltammetry

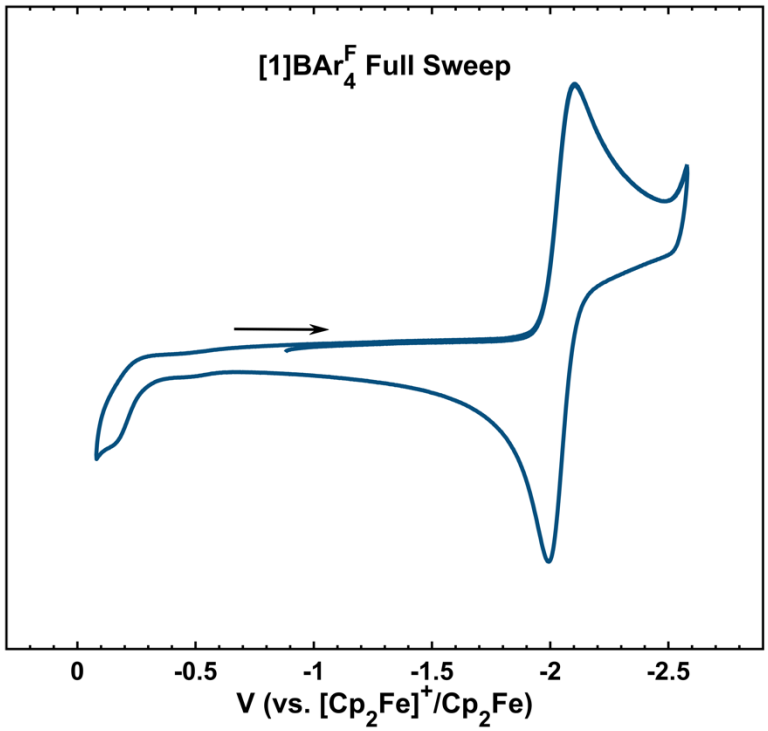

Figure S31. Cyclic voltammogram of [**1**]BAr$^F_4$ (0.1 M [^{n}Pr$_4$N]BAr$^F_4$ in THF, scan rate = 250 mV·s^{-1}, collected under Ar).

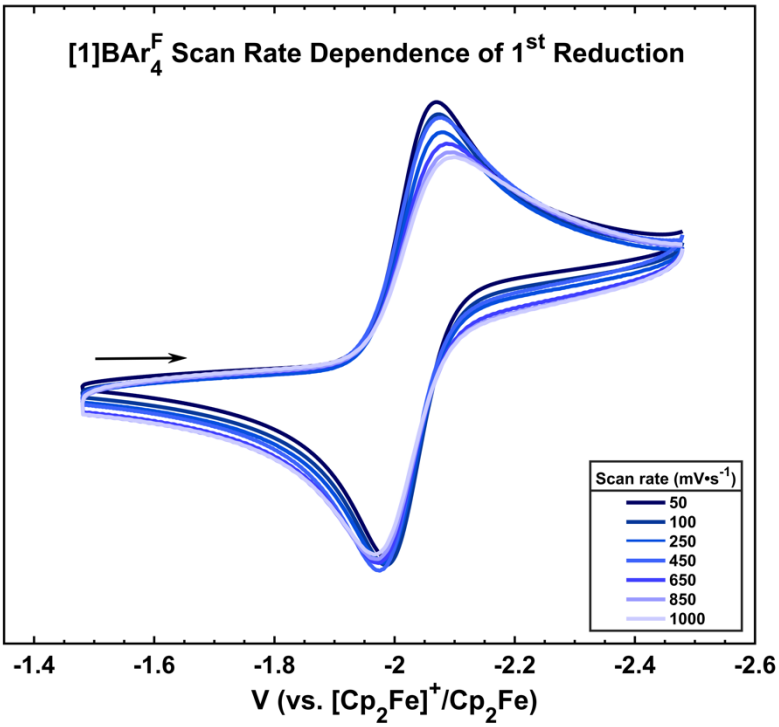

Figure S32. Overlay of CV scans at various scan rates for [**1**]BAr$^F_4$ (0.1 M [^{n}Pr$_4$N]BAr$^F_4$ in THF, collected under Ar). Current values are normalized by dividing by the square root of scan rate.

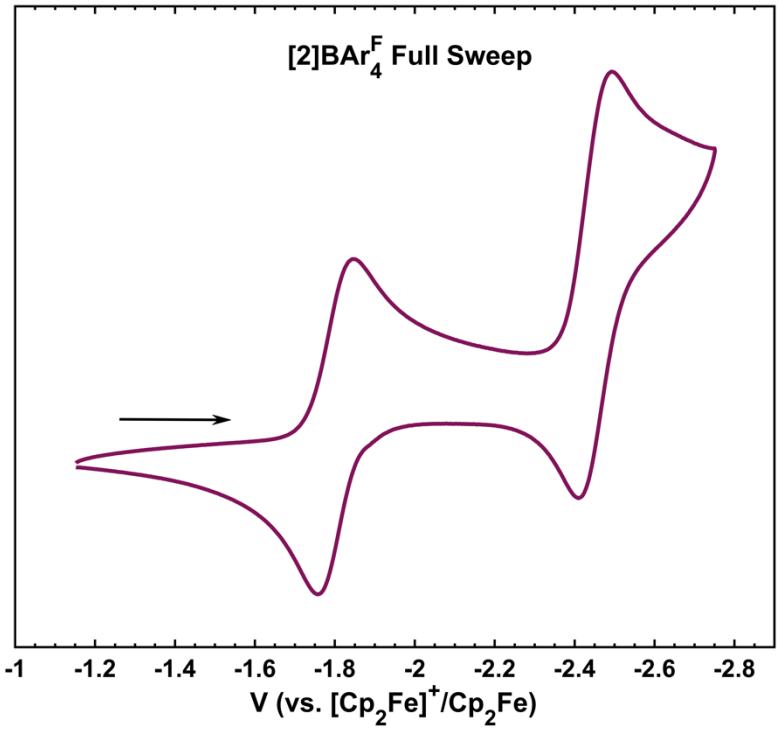

Figure S33. Cyclic voltammogram of [**2**]BAr^F_4 (0.1 M [^{n}Pr$_4$N]BAr^F_4 in THF, scan rate = 250 mV·s^{-1}, collected under Ar).

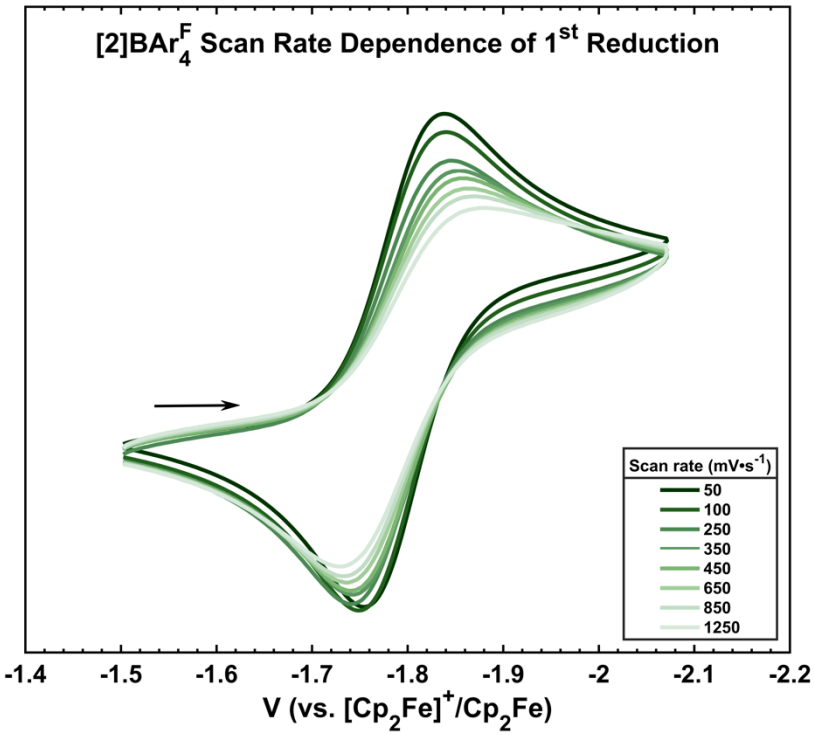

Figure S34. Overlay of CV scans centered at the first reduction process at various scan rates for [**2**]BAr^F_4 (0.1 M [^{n}Pr$_4$N]BAr^F_4 in THF, collected under Ar). Current values are normalized by dividing by the square root of scan rate.

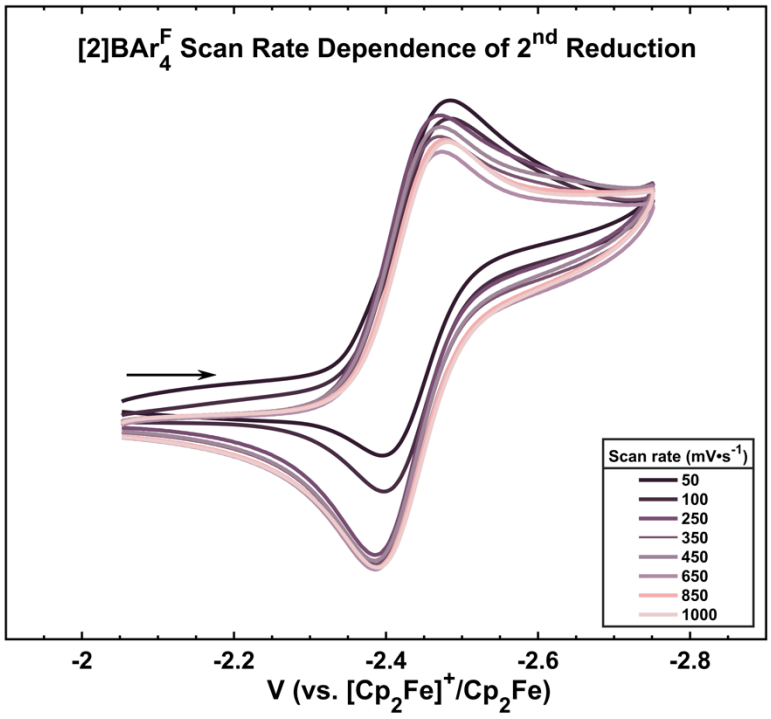

Figure S35 Overlay of CV scans centered at the second reduction process at various scan rates for [**2**]BAr^F_4 (0.1 M [^{n}Pr$_4$N]BAr^F_4 in THF, collected under Ar). Current values are normalized by dividing by the square root of scan rate.

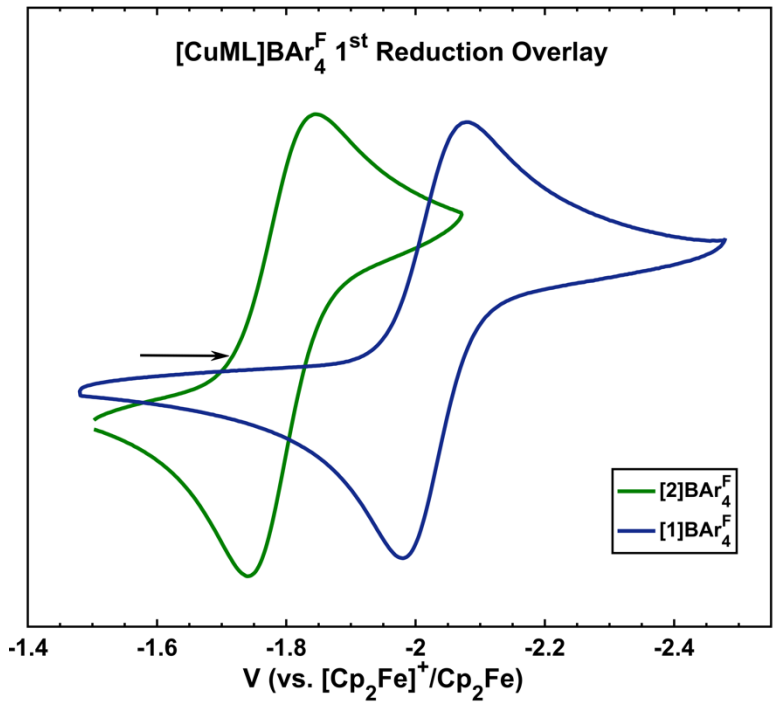

Figure S36. Overlay of cyclic voltammograms of [**1**]BAr^F_4 and [**2**]BAr^F_4 (0.1 M [^{n}Pr$_4$N]BAr^F_4 in THF, scan rate = 250 mV·s^{-1}, collected under Ar).

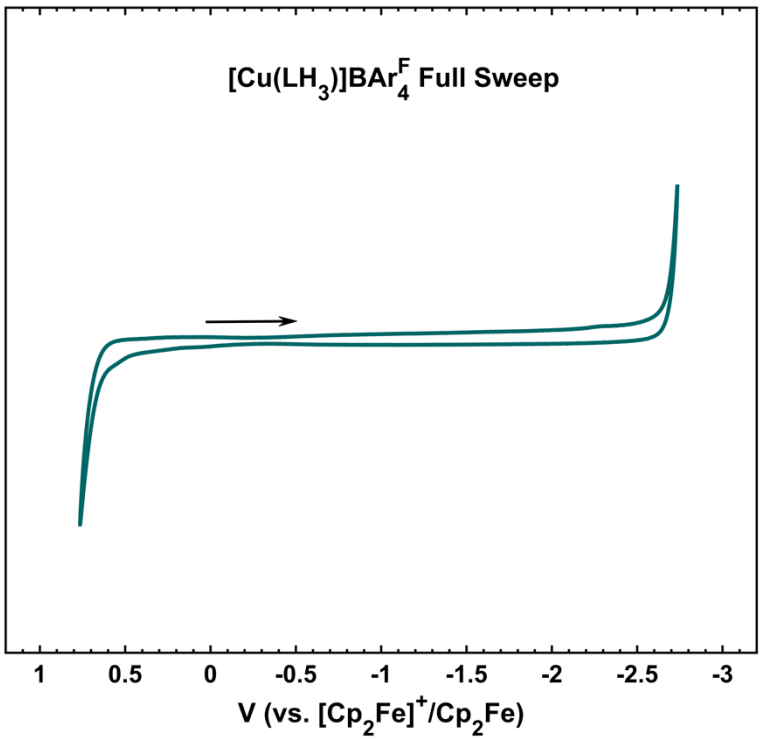

Figure S37. Cyclic voltammogram of [**Cu(LH$_3$)**]BAr$^F{}_4$ (0.1 M [^{n}Pr$_4$N]BAr$^F{}_4$ in THF, scan rate = 250 mV·s^{-1}, collected under Ar).

UV-vis Spectroscopy

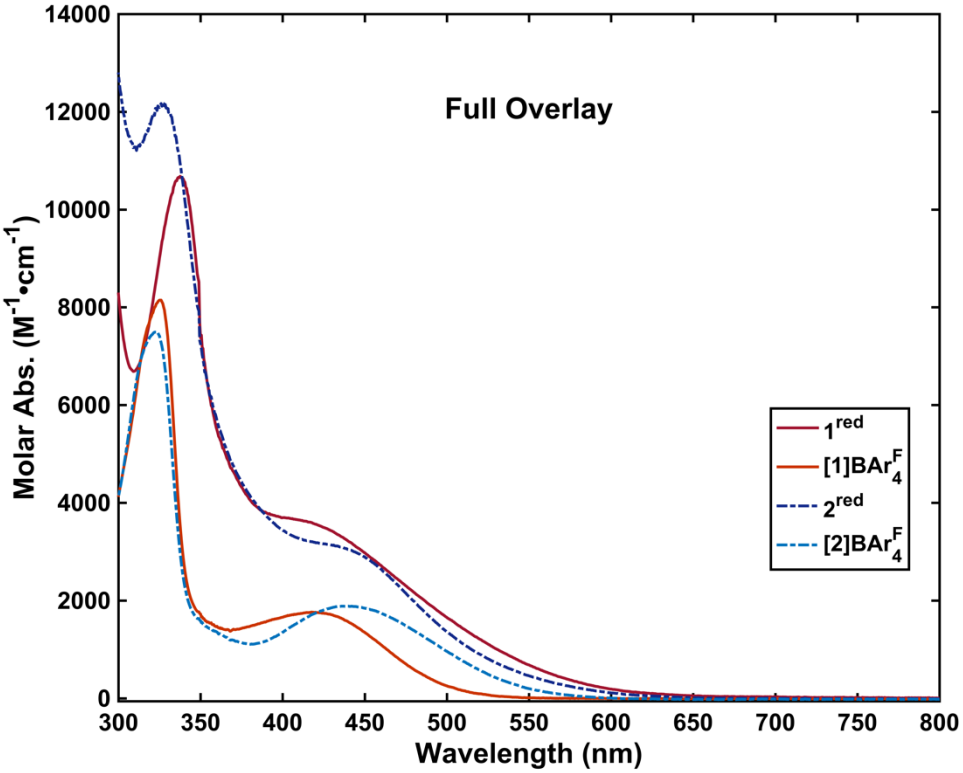

Figure S38. UV-vis spectra of [**1**]BAr^F_4, [**2**]BAr^F_4, $\mathbf{1}^{red}$, and $\mathbf{2}^{red}$ (0.25 mM in toluene).

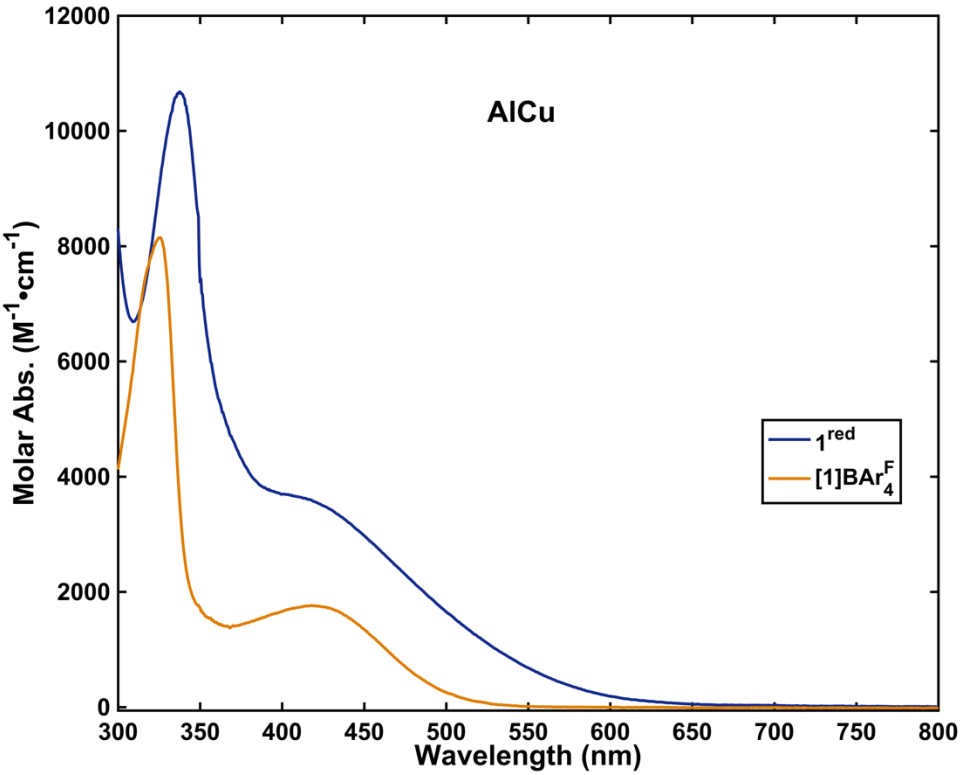

Figure S39. UV-vis spectra of [**1**]BAr^F_4 (orange trace) and $\mathbf{1}^{red}$ (blue trace) (0.25 mM in toluene).

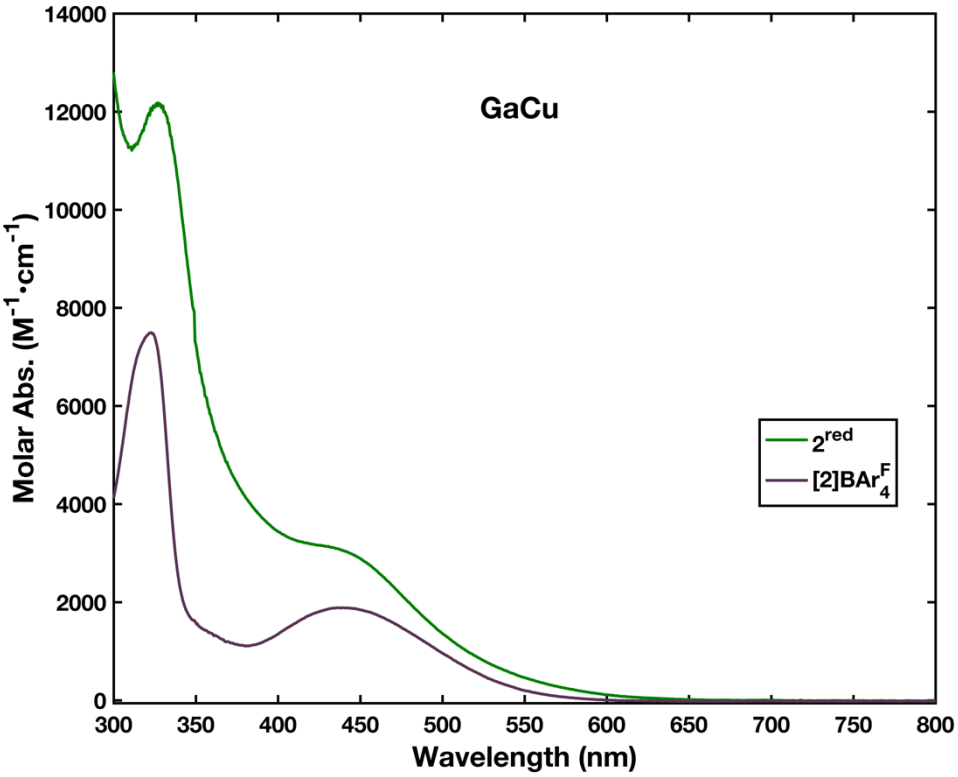

Figure S40. UV-vis spectra of [**2**]BAr^{F}_{4} (purple trace) and **2**^{red} (green trace) (0.25 mM in toluene).

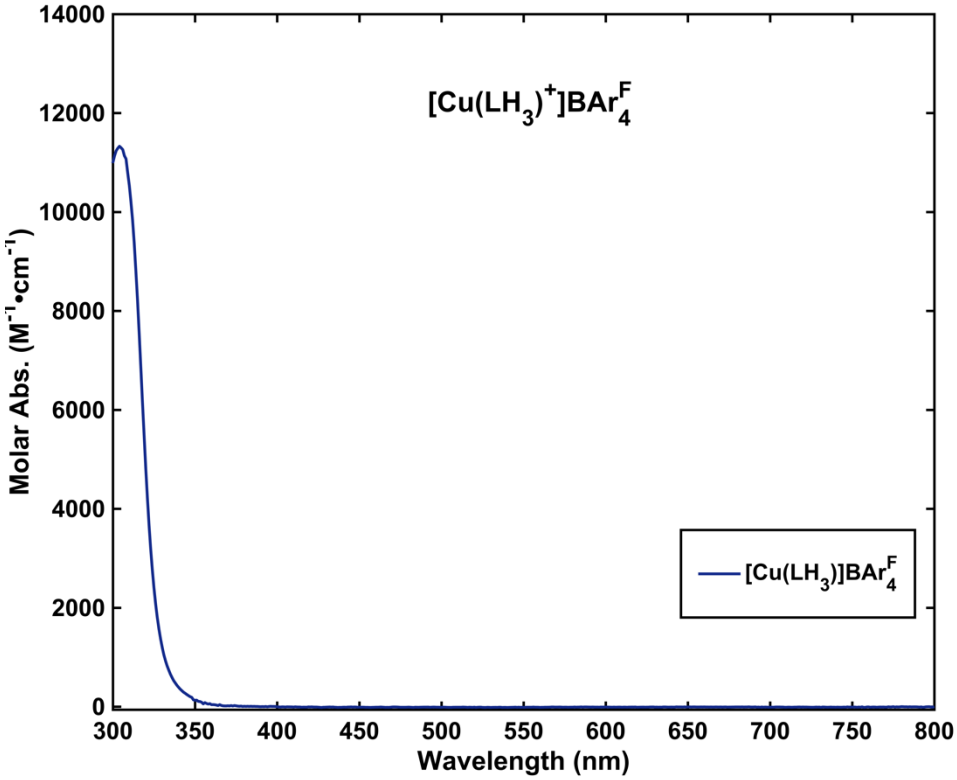

Figure S41. UV-vis spectrum of [**Cu(LH$_3$)**]BAr^{F}_{4} (0.25 mM in toluene).

EPR Spectroscopy

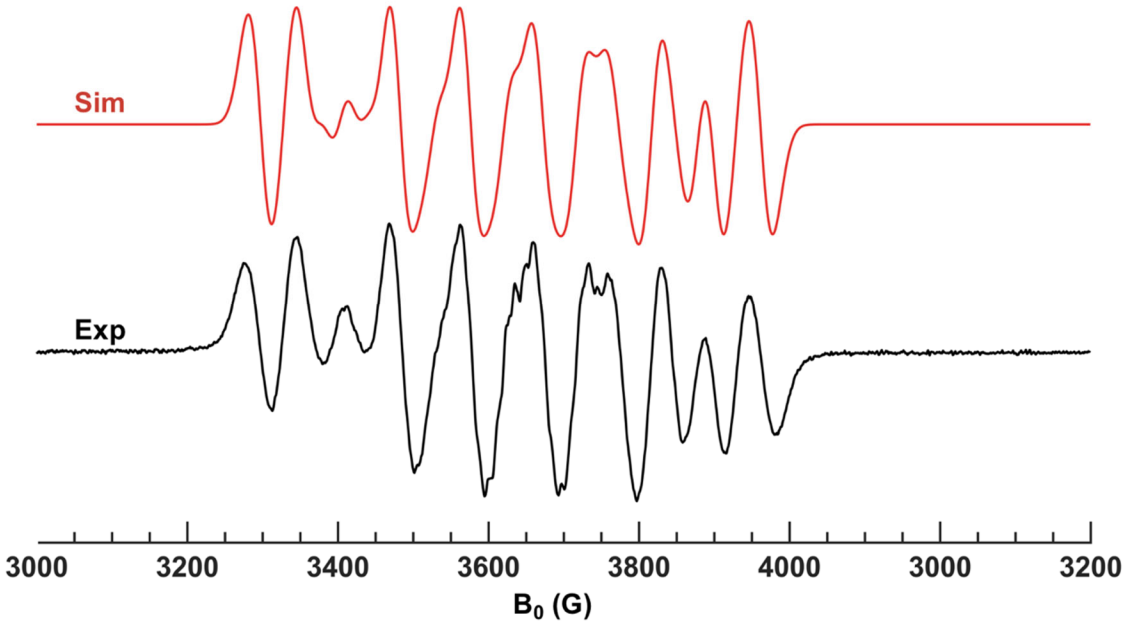

Figure S42. X-band EPR spectrum of a 2.5 mM solution of **1**^{red} taken at 298 K in a 1:1 mixture of 2-MeTHF/toluene (black) and corresponding simulation (red). Experimental parameters: frequency = 9.645857 GHz, center field = 3500 G, sweep width = 1400 G, modulation amplitude = 9.81 G, resolution = 2048 data points, microwave power = 0.67 mW, power attenuation = 20 dB, line widths = 2.45 MHz. Simulation parameters (garlic): g = 2.007, A(^{27}Al) = 269.7 MHz, A(^{63}Cu)= 171.4 MHz, A(^{65}Cu) = 182.6 MHz, line widths = 2.45 MHz.

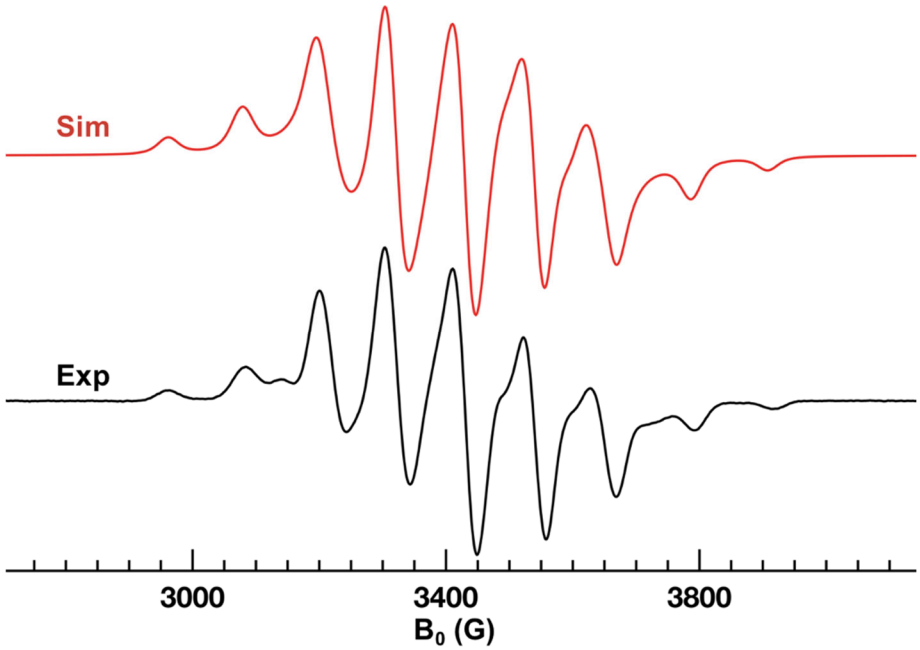

Figure S43. X-band EPR spectrum of a 2.0 mM solution of **1**^{red} taken at 45 K in a 1:1 mixture of 2-MeTHF/toluene (black) and corresponding simulation (red). Experimental parameters: microwave frequency = 9.647866 GHz, center field = 3500 G, sweep width = 1800 G, modulation amplitude = 5.0 G, resolution = 2048 data points, microwave power = 0.2 mW, power attenuation = 30 dB, line widths = 2.50 MHz. Simulation parameters (pepper): g = [2.005, 2.005, 2.007], A(^{27}Al) = [229.6, 229.6, 325.4] MHz, A(^{63}Cu) = [56.2, 56.2, 341.6] MHz, A(^{65}Cu) = [60.1, 60.1, 365.3] MHz,

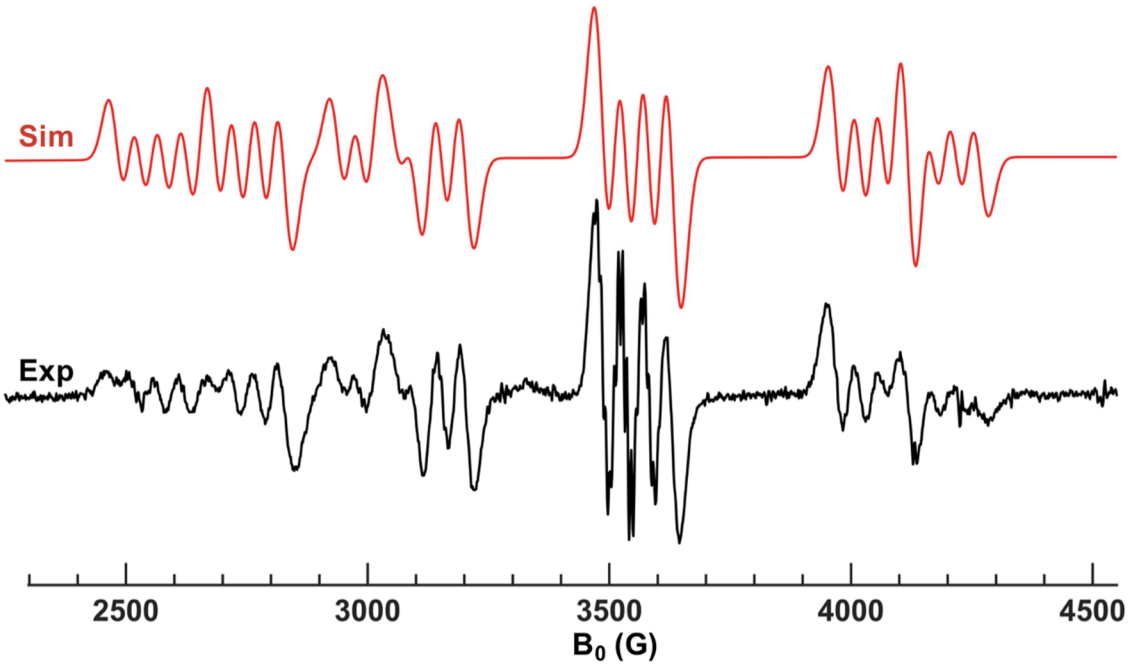

Figure S44. X-band EPR spectrum of a 2.5 mM solution of **2**^{red} taken at 298 K in a 1:1 mixture of 2-MeTHF/toluene (black) and corresponding simulation (red). Experimental parameters: frequency = 9.639385 GHz, center field = 3500 G, sweep width = 3000 G, modulation amplitude = 5 G, resolution = 2048 data points, microwave power = 21.3 mW, power attenuation = 10 dB, line widths = 3.58 MHz. Simulation parameters (garlic): g = 2.002; A(^{63}Cu) = 128.9 MHz, A(^{65}Cu) = 137.3 MHz, A(^{69}Ga) = 1199.3 MHz, A(^{71}Ga)= 1524.3 MHz, A(^{31}P)×3 = 29.4 MHz, A(^{14}N)×3 = 20.1 MHz, line widths = 3.80 MHz

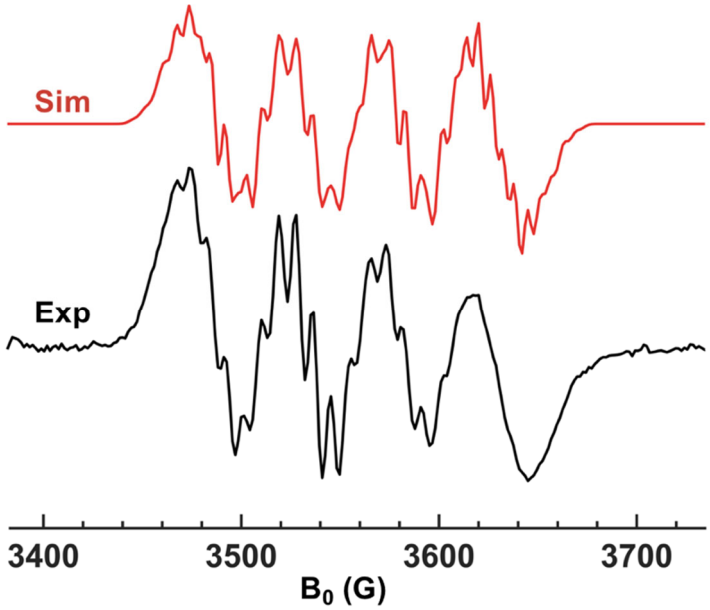

Figure S45. Zoom of the X-band EPR spectrum of a 2.5 mM solution of **2**^{red} taken at 298 K in a 1:1 mixture of 2-MeTHF/toluene showing the $m_I = -1/2$ transition (black) and corresponding simulation (red). Experimental parameters: frequency = 9.639385 GHz, center field = 3500 G, sweep width = 3000 G, modulation amplitude = 5 G, resolution = 2048 data points, microwave power = 21.3 mW, power attenuation = 10 dB, line widths = 0.51 MHz. This model is isolated to the $m_I = -1/2$ transition as it introduces unrealistic resolution/hyperfine coupling to the remaining signals. Simulation parameters (garlic): g = 2.002; A(^{63}Cu) = 128.9 MHz, A(^{65}Cu) = 137.3 MHz, A(^{69}Ga) = 1199.3 MHz, A(^{71}Ga)= 1524.3 MHz, A(^{31}P)×3 = 29.4, A(^{14}N)×3 = 19.9, MHz, line widths = 0.35 MHz

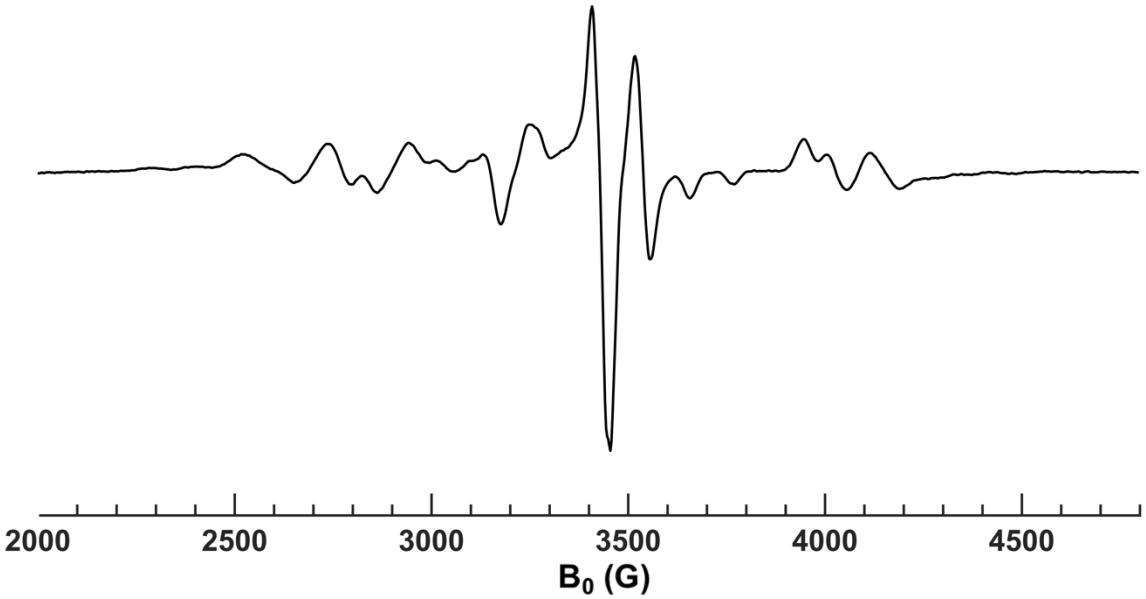

Figure S46. X-band EPR spectrum of a 2.0 mM solution of **2**^{red} taken at 35 K in a 1:1 mixture of 2-MeTHF/toluene (black). Experimental parameters: frequency = 9.648873 GHz, center field = 3400 G, sweep width = 2800 G, modulation amplitude = 9.81 G, resolution = 2048 data points, microwave power = 0.2 mW, power attenuation = 30 dB, conversion time = 703 ms, line widths = 4.0 MHz. Simulations of this spectra were unsuccessful. At standard conversion times (ca. 20 ms) signal was nearly unobservable. Only as very long conversion time (ca. 700 ms) was this signal observed.

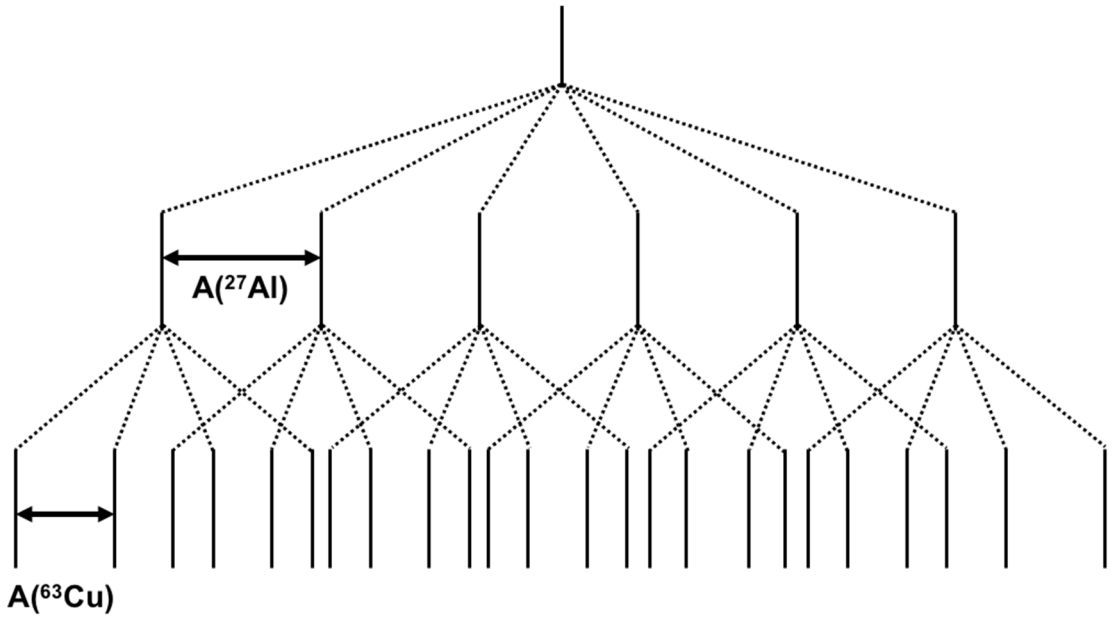

Figure S47. Splitting tree diagram derived from simulated hyperfine couplings for **1**^{red} showing general coupling between ^{27}Al (I = 5/2) and ^{63}Cu (I = 3/2) nuclei. A similar diagram would arise from the ^{65}Cu couplings. Note: the broadness of the experimental spectrum prohibits resolving all peaks.

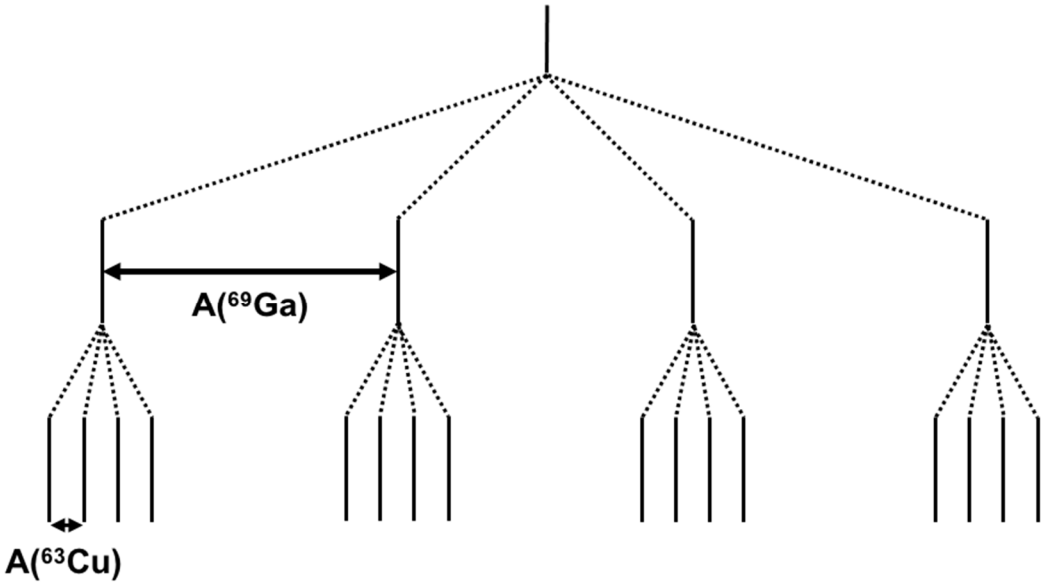

Figure S48. Splitting tree diagram derived from simulated hyperfine couplings for **2**^{red} showing general coupling between ^{69}Ga (I = 3/2) and ^{63}Cu (I = 3/2) nuclei. A similar diagram would arise from the ^{71}Ga and ^{65}Cu couplings.

Experimental spin density calculation. Using the low temperature EPR spectrum of **1**^{red}, the spin density can be estimated from the experimental data. Decomposition of the hyperfine tensors of the spin-active nuclei into their isotropic (eq. 1) and anisotropic (eq. 2) can be achieved by using the equations below. Once calculated, the experimental values can then be compared to those tabulated in the literature.[16]

$$A_{\mathrm{iso}} = \frac{1}{3}\left(\mathrm{A_x} + \mathrm{A_y} + \mathrm{A_z}\right) \quad (1)$$

$$\boldsymbol{b} = \left[(\mathrm{A_x} - \mathrm{A_{iso}}), (\mathrm{A_y} - \mathrm{A_{iso}}), (\mathrm{A_z} - \mathrm{A_{iso}})\right] \quad (2)$$

An example set of calculations are shown for ^{27}Al to calculate the spin density residing in the 3s and 3p$_z$ orbitals (eqs. 3–6). Although the Al/Cu np$_z$ and Cu 3d$_{z^2}$ orbitals have the same symmetry, strong evidence of for p$_z$ can be implied based on computational data and the d^{10} of the Cu(I) ion prior to reduction.

$$\mathrm{A_{iso}}\left(^{27}\mathrm{Al}\right) = \frac{1}{3}(229.6 + 229.6 + 325.4) = 261.5\ \mathrm{MHz} \quad (3)$$

$$\mathrm{A_{iso}}\left(^{27}\mathrm{Al}\right) = \frac{1}{3}(229.6 + 229.6 + 325.4) = 261.5\ \mathrm{MHz}$$

$$\boldsymbol{b}\left(^{27}\mathrm{Al}\right) = [(229.6 - 261.5), (229.6 - 261.5), (325.4 - 261.5)] = [-32, -32, 64] \quad (4)$$

$$\mathrm{Al}_{3s} = \frac{A_{iso}(^{27}\mathrm{Al})}{A^{0}_{iso}(^{27}\mathrm{Al})} = \frac{261.5}{3911} = 0.066 \quad (5)$$

$$\mathrm{Al}_{3p_z} = \frac{\boldsymbol{b}(^{27}\mathrm{Al})}{\boldsymbol{b^0}\,(^{27}\mathrm{Al})} = \frac{[-32,-32,64]}{[-83,-83,166]} = 0.385 \quad (6)$$

Computational Section

Methods

Geometry Optimizations. Full geometry optimizations were performed using Kohn-sham density functional theory (KS-DFT) with the M06-L functional[17] with the def2-TZVPP basis set for the Cu, Al, and Ga atoms, def2-TZVP basis for N and P atoms, and def2-SVP for C and H atoms.[18] Calculations were in the gas phase and performed with the Gaussian 16 software.[19] Additionally, vibrational frequency calculations were performed to confirm that each optimized structure was a stationary point on the potential energy surface.

EPR Calculation. EPR parameters (g-tensors) and hyperfine/superhyperfine coupling constants (A-tensors) were computed with the ORCA 5.0.0 software.[20, 21] Based on the in depth study by Hedegård et al.[22], the PBE0[23, 24] functional was used to determine the EPR parameters. These calculations were performed with the relativistic def2-TZVP[18] basis set for all atoms and the Wiegend J auxiliary basis sets[25] (def2/J) found in ORCA. Relativistic effects were included by the ZORA (zeroth-order regular approximation) formalism.[26] Additional calculations were performed with the TPSSh[27] functional with no relativistic effects and the def2/J basis set from ORCA for comparison.

Two of the elements Cu and Ga have two naturally abundant isotopes, ^{63}Cu/^{65}Cu. And ^{69}Ga/^{71}Ga. The calculation of EPR parameters only yield the A-tensors of the most abundant nuclei (^{63}Cu and ^{69}Ga). To derive the coupling value associated with the less abundant nuclei (^{65}Cu and ^{71}Ga), the A-tensor can be multiplied by a factor, σ, calculated from the gyromagnetic ratios of the two isotopes. The calculations below show how σ is calculated for both Cu (eq. 7) and Ga (eq. 8), where μ is the magnetic moment (in units of nuclear magneton, μ_N) and I is the nuclear spin. Magnetic moment values were obtained from the work of Stone.[28]

$$\sigma_{Cu} = \frac{\mu_{^{65}Cu}/I_{^{65}Cu}}{\mu_{^{63}Cu}/I_{^{63}Cu}} = \frac{(2.38162/1.5)}{(2.22734/1.5)} = 1.06922 \quad (7)$$

$$\sigma_{Ga} = \frac{\mu_{^{71}Ga}/I_{^{71}Ga}}{\mu_{^{69}Ga}/I_{^{69}Ga}} = \frac{(2.56227/1.5)}{(2.01659/1.5)} = 1.27060 \quad (8)$$

TD-DFT Calculations. Single point energies on the optimized geometries from M06-L were computed using time-dependent DFT (TD-DFT). The M06-L functional[17] with the def2-TZVPP basis set for the Cu, Al, and Ga atoms, def2-TZVP basis for N and P atoms, and def2-SVP for C and H atoms[18] were used.

Table S3. Selected bond lengths (Å) and angles (deg) for optimized structures of $\mathbf{1}^{red}$ and $[\mathbf{1}]^+$ and their corresponding experimental crystal structures. Differences in bond lengths and angles between the charged and neutral species are reported for both theory and experiment.

Parameter	$\mathbf{1}^{red}$		$[\mathbf{1}]^+$		Diff. ($\mathbf{1}^{red}$–$[\mathbf{1}]^+$)	
(Å or °)	Exp.	M06-L	Exp.	M06-L	Exp.	M06-l
Al–Cu	2.530	2.551	2.624	2.693	-0.094	-0.142
Cu–P	2.251	2.271	2.292	2.318	-0.041	-0.047
Al–N_{Eq}	1.891	1.895	1.853	1.853	0.038	0.042
Al–N_{Apical}	2.084	2.090	2.002	1.970	0.082	0.120
∠P–Cu–P	119.5	119.6	119.3	119.3	0.2	0.3
∠N_{Eq}–Al–N_{Eq}	117.4	118.5	119.8	119.9	-2.4	-1.4

Table S4. Selected bond lengths (Å) and angles (deg) for optimized structures of $\mathbf{2}^{red}$ and $[\mathbf{2}]^+$ and their corresponding experimental crystal structures. Differences in bond lengths and angles between the charged and neutral species are reported for both theory and experiment.

Parameter	$\mathbf{2}^{red}$		$[\mathbf{2}]^+$		Diff. ($\mathbf{2}^{red}$–$[\mathbf{2}]^+$)	
(Å or °)	Exp.	M06-L	Exp.	M06-L	Exp.	M06-l
Ga–Cu	2.454	2.516	2.574	2.673	-0.120	-0.157
Cu–P	2.269	2.297	2.299	2.332	-0.030	-0.035
Ga–N_{Eq}	1.962	1.972	1.905	1.917	0.057	0.055
Ga–N_{Apical}	2.194	2.222	2.074	2.056	0.120	0.166
∠P–Cu–P	118.4	119.3	119.4	119.3	-1.0	0.0
∠N_{Eq}–Ga–N_{Eq}	116.4	117.0	119.4	119.5	-3.0	-2.5

Table S5. Energies of selected molecular orbitals of [**Cu(LH$_3$)**]$^+$ obtained using TD-DFT and the M06-L functional.

Orbital	Energy (eV)	Assignment	Composition (%)
LUMO	–3.78	–	**Cu** 29.1 (4p), **P** 35.2 (3p)
HOMO–4	–8.14	Cu d_{xy}/d_{x2-y2}	**Cu** 39.7 (3d), **P** 33.7 (3p)
HOMO–5	–8.14	Cu d_{xy}/d_{x2-y2}	**Cu** 39.6 (3d), **P** 30.0 (3p)
HOMO–8	–8.93	Cu d_{z2}	**Cu** 87.7 (3d 79.7, 4s 8.0)
HOMO–9	–9.17	Cu d_{xz}/d_{yz}	**Cu** 95.1 (3d)
HOMO–10	–9.17	Cu d_{xz}/d_{yz}	**Cu** 95.1 (3d)

Table S6. Energies of selected molecular orbitals of [**1**]$^+$ obtained using TD-DFT and the M06-L functional.

Orbital	Energy (eV)	Assignment	Composition (%)
LUMO	–4.73	–	**Cu** 19.7 (4p), **Al** 30.7 (17.0 3s, 13.7 3p), **P** 17.2 (3p)
HOMO–4	–8.38	Cu d_{xy}/d_{x2-y2}	**Cu** 28.6 (3d), **P** 38.9 (3p)
HOMO–5	–8.38	Cu d_{xy}/d_{x2-y2}	**Cu** 28.6 (3d), **P** 38.7 (3p)
HOMO–8	–8.66	Cu d_{z2}	**Cu** 54.2 (3d 46.7, 4p 7.4), **N** 9.8 (2p)
HOMO–9	–9.88	Cu d_{xz}/d_{yz}	**Cu** 81.9 (3d)
HOMO–10	–9.88	Cu d_{xz}/d_{yz}	**Cu** 81.9 (3d)

Table S8. Energies of selected molecular orbitals of **1**^{red} obtained using TD-DFT and the M06-L functional.

Orbital	Energy (eV)	Assignment	Composition (%)
SOMO	–2.61	–	**Cu** 8.4 (4p). **Al** 33.8 (19.0 3s, 14.8 3p), **P** 35.2 (3p)
SOMO–4	–5.44	Cu d_{xy}/d_{x2-y2}	**Cu** 35.7 (3d) **P** 31.8 (3p)
SOMO–5	–5.44	Cu d_{xy}/d_{x2-y2}	**Cu** 35.7 (3d) **P** 34.4 (3p)
SOMO–9	–6.56	Cu d_{z2}	**Cu** 53.7 (3d), **N** 6.8 (2p)
SOMO–10	–6.64	Cu d_{xz}/d_{yz}	**Cu** 85.3 (3d)
SOMO–11	–6.64	Cu d_{xz}/d_{yz}	**Cu** 85.3 (3d)

Table S9. Energies of selected molecular orbitals of [**2**]$^{+}$ obtained using TD-DFT and the M06-L functional.

Orbital	Energy (eV)	Assignment	Composition (%)
LUMO	–4.95	–	**Cu** 23.5 (4p), **Ga** 30.3 (17.7 4s, 12.6 4p), **P** 17.8 (3p)
HOMO–4	–8.46	Cu d_{xy}/d_{x2-y2}	**Cu** 29.2 (3d), **P** 36.3 (3p)
HOMO–5	–8.46	Cu d_{xy}/d_{x2-y2}	**Cu** 29.1 (3d), **P** 35.5 (3p)
HOMO–12	–9.93	Cu d_{xz}/d_{yz}	**Cu** 82.4 (3d)
HOMO–13	–9.93	Cu d_{xz}/d_{yz}	**Cu** 82.4 (3d)
HOMO–14	–9.99	Cu d_{z2}	**Cu** 53.5 (3d 47.8, 4s 5.7), **N** 7.9 (2p)

Table S10. Energies of selected molecular orbitals of $\mathbf{2}^{red}$ obtained using TD-DFT and the M06-L functional.

Orbital	Energy (eV)	Assignment	Composition (%)
SOMO	–2.88	–	**Cu** 12.7 (4p), **Ga** 32.0 (18.7 4s, 13.3 4p), **P** 35.2 (3p)
SOMO–5	–5.55	Cu d_{xy}/d_{x2-y2}	**Cu** 36.7 (3d), **P** 31.7 (3p)
SOMO–6	–5.55	Cu d_{xy}/d_{x2-y2}	**Cu** 36.1 (3d), **P** 34.1 (3p)
SOMO–13	–6.75	Cu d_{xz}/d_{yz}	**Cu** 77.7 (3d)
SOMO–14	–6.75	Cu d_{xz}/d_{yz}	**Cu** 77.5 (3d)
SOMO–15	–6.97	Cu d_{z2}	**Cu** 56.1 (3d), **Ga** 5.2 (4p)

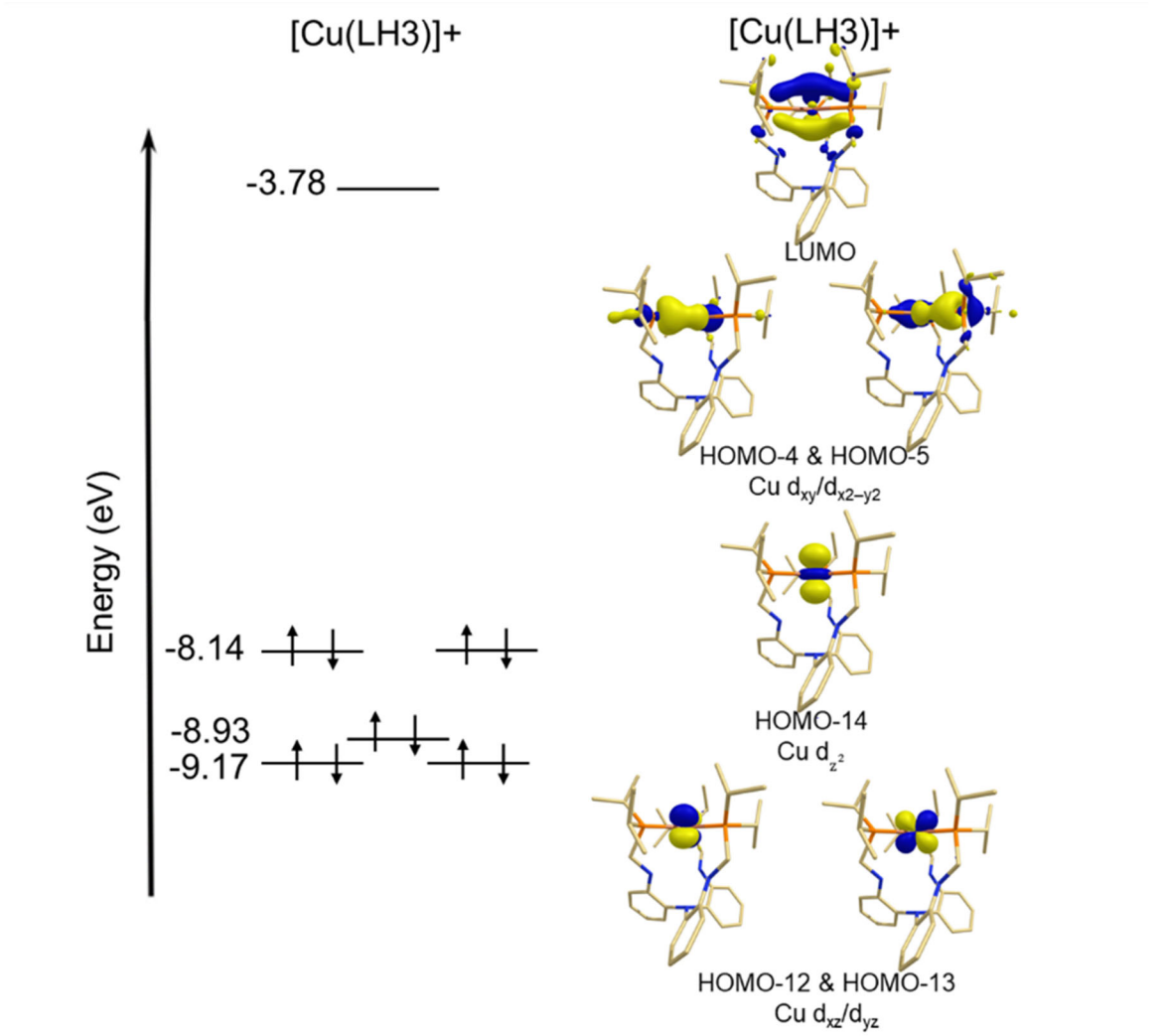

Figure S49. Molecular orbital energy diagram of $[\mathbf{Cu(LH_3)}]^+$ as calculated with M06-L. Selected molecular orbitals are shown.

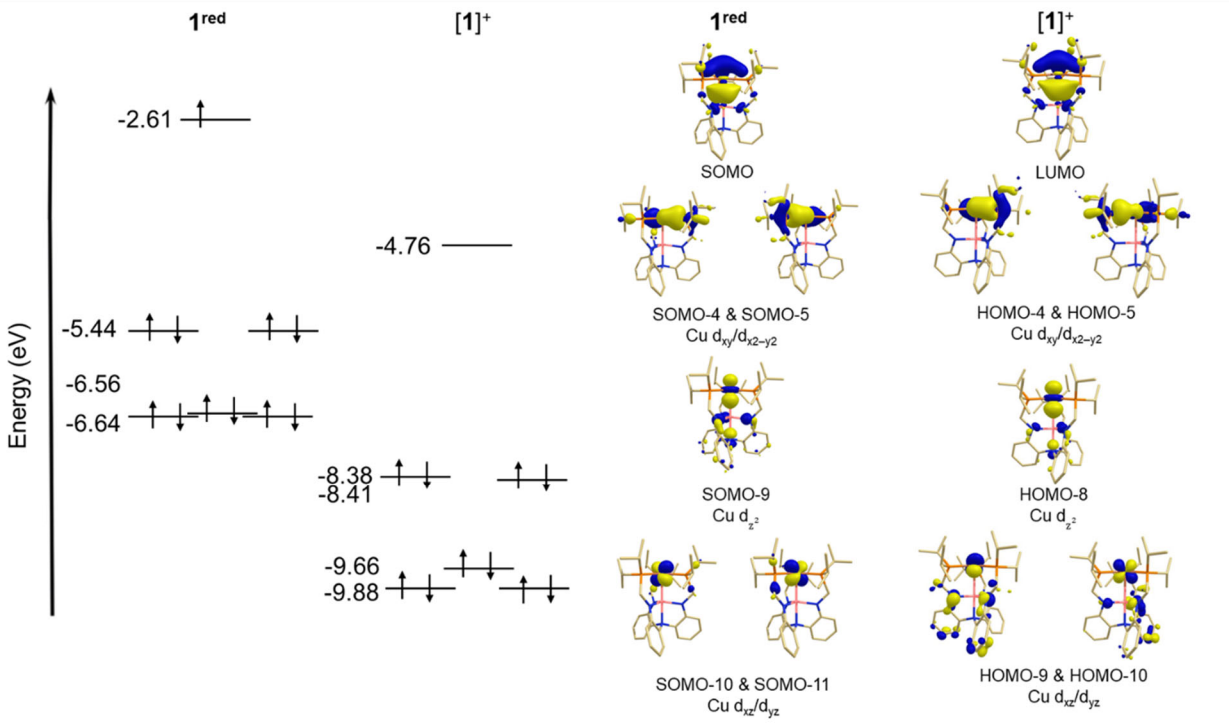

Figure S50. Molecular orbital energy diagram of **1**^{red} and [**1**]$^{+}$ as calculated with M06-L. Selected molecular orbitals are shown.

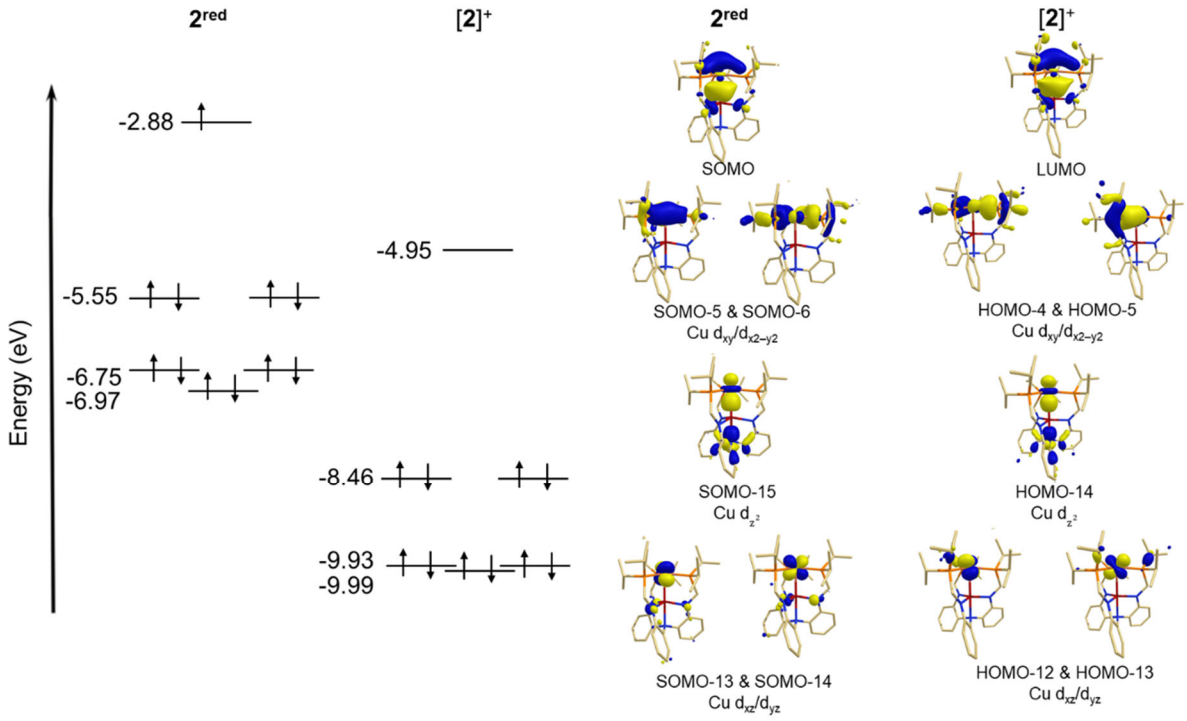

Figure S51. Molecular orbital energy diagram of **2**^{red} and [**2**]$^{+}$ as calculated with M06-L. Selected molecular orbitals are shown.

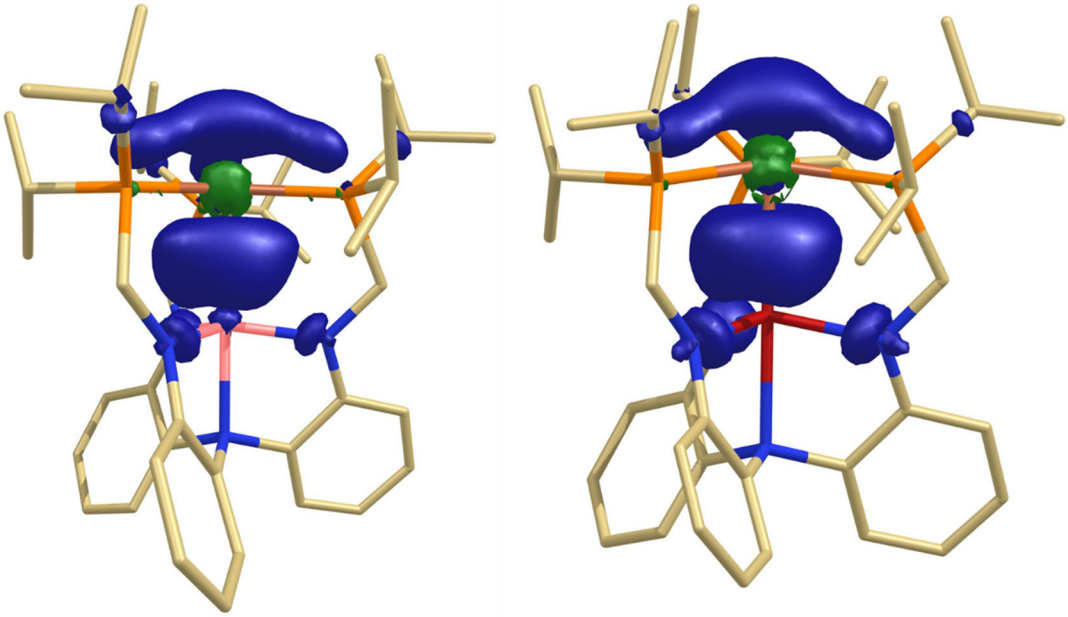

Figure S52. Spin density plots of the neutral species $\mathbf{1}^{red}$ and $\mathbf{2}^{red}$ with the blue surface corresponding to an excess of α-electron density and the green surface corresponding to an excess of β-electron density.

Table S11. Mulliken spin densities of copper, phosphorous and either gallium or aluminum for the neutral species computed using the Mulliken charge analysis method with M06-L.

Orbital	$\mathbf{1}^{red}$	$\mathbf{2}^{red}$
Al/Ga	0.52	0.44
Cu	0.18	0.24
P	0.09	0.08
N	0.01	0.03
3P	0.27	0.24
3N	0.03	0.09
CuP_3	0.45	0.48
MN_3	0.55	0.53

Table S12. DFT-calculated EPR parameters computed with PBE0 functional. The hyperfine splittings are in MHz. Factors for proportionality (σ) for Ga and Cu are 1.27060 and 1.06922 respectively.

1^{red}			**2^{red}**		
Parameter	**Theory**	**Exp.**	**Parameter**	**Theory**	**Exp.**
g	2.005	2.007	g	2.003	2.002
A(^{63}Cu)	129 [44, 44, 299]	171.4 [56, 56 , 341.6]	A(^{63}Cu)	108 [31, 31, 261]	128.9 –
A(^{65}Cu)	138 [47, 47, 320]	182.6 [60, 60, 365]	A(^{65}Cu)	118 [33, 33, 279]	137.3 –
A(^{27}Al)	272 [250, 250, 317]	269.7 [230, 230, 325]	A(^{69}Ga)	1344 [1283, 1283, 1466]	1199.3 –
–	–	–	A(^{71}Ga)	1708 [1628, 1628, 1861]	1524.3 –
A(^{31}P)^{b}	51 [30, 56, 68]	–	A(^{31}P)^{b}	45 [24, 50, 61]	29.4 –
A(^{14}N$_{Eq}$)^{b}	18 [17, 17, 20]	–	A(^{14}N$_{Eq}$)^{b}	26 [24, 24, 30]	20.1 –

[a]Values in brackets are anisotropic hyperfine coupling components. [b]Average of 3 values.

Table S13. DFT-calculated EPR parameters computed with TPSSh functional. The hyperfine splittings are in MHz. Factors for proportionality (σ) for Ga and Cu are 1.27060 and 1.06922 respectively.

1^{red}			**2^{red}**		
Parameter	**Theory**	**Exp.**	**Parameter**	**Theory**	**Exp.**
g	2.005	2.007	g	2.01	2.002
A(^{63}Cu)	149 [80, 80, 289]	171.4 [56, 56 , 341.6]	A(^{63}Cu)	123 [68, 165, 135.7]	128.9 –
A(^{65}Cu)	159 [86, 86, 309]	182.6 [60, 60, 365]	A(^{65}Cu)	132 [72, 176, 145]	137.3 –
A(^{27}Al)	228 [208, 208, 267]	269.7 [230, 230, 325]	A(^{69}Ga)	1130 [1089, 1160, 1139]	1199.3 –
–	–	–	A(^{71}Ga)	1435 [1384, 1474, 1441]	1524.3 –
A(^{31}P)	40 [25, 48, 48]	–	A(^{31}P)^{b}	34 [39, 29, 32]	29.4 –
A(^{14}N$_{Eq}$)	21 [20, 21, 21]	–	A(^{14}N$_{Eq}$)^{b}	28 [29, 28, 28]	20.1 –

[a]Values in brackets are anisotropic hyperfine coupling components. [b]Average of 3 values.

References

1. S. Stoll and A. Schweiger, *J. Magn. Reson.*, 2006, **178**, 42-55.
2. P. A. Rudd, S. Liu, L. Gagliardi, V. G. Young, Jr. and C. C. Lu, *J. Am. Chem. Soc.*, 2011, **133**, 20724-20727.
3. R. C. Cammarota and C. C. Lu, *J. Am. Chem. Soc.*, 2015, **137**, 12486-12489.
4. R. K. Thomson, B. L. Scott, D. E. Morris and J. L. Kiplinger, *Comptes Rendus Chimie*, 2010, **13**, 790-802.
5. T. Tsuda, T. Yazawa, K. Watanabe, T. Fujii and T. Saegusa, *J. Org. Chem.*, 1981, **46**, 192-194.
6. M. Brookhart, B. Grant and A. F. Volpe, *Organometallics*, 2002, **11**, 3920-3922.
7. W. Gu and O. V. Ozerov, *Inorg. Chem. Commun.*, 2011, **50**, 2726-2728.
8. D. E. Bergbreiter and J. M. Killough, *J. Am. Chem. Soc.*, 2002, **100**, 2126-2134.
9. R. H. Blessing, *Acta Crystallogr. A*, 1995, **51 (Pt 1)**, 33-38.
10. G. M. Sheldrick, *Acta Crystallogr. A* 2015, **71**, 3-8.
11. C. B. Hubschle, G. M. Sheldrick and B. Dittrich, *J. Appl. Crystallogr.*, 2011, **44**, 1281-1284.
12. G. M. Sheldrick, *Acta Crystallogr. C*, 2015, **71**, 3-8.
13. A. L. Spek, *Acta Crystallogr. D*, 2009, **65**, 148-155.
14. B. Cordero, V. Gomez, A. E. Platero-Prats, M. Reves, J. Echeverria, E. Cremades, F. Barragan and S. Alvarez, *Dalton Trans.*, 2008, 2832-2838.
15. *Persistence of Vision Pty. Ltd.*, 2004.
16. J. R. Morton and K. F. Preston, *J. Magn. Reson.*, 1978, **30**, 577-582.
17. Y. Zhao and D. G. Truhlar, *J. Chem. Phys.*, 2006, **125**, 194101.
18. F. Weigend and R. Ahlrichs, *Phys. Chem. Chem. Phys.*, 2005, **7**, 3297-3305.
19. M. J. T. Frisch, G. W.; Schlegel, H. B.; Scuseria, G. E.; Robb, M. A.; Cheeseman, J. R.; Scalmani, G.; Barone, V.; Mennucci, B.; Petersson, G. A.; Nakatsuji, H.; Caricato, M.; Li, X.; Hratchian, H. P.; Izmaylov, A. F.; Bloino, J.; Zheng, G.; Sonnenberg, J. L.; Hada, M.; Ehara, M.; Toyota, K.; Fukuda, R.; Hasegawa, J.; Ishida, M.; Nakajima, T.; Honda, Y.; Kitao, O.; Nakai, H.; Vreven, T.; Montgomery, J. A., Jr.; Peralta, J. E.; Ogliaro, F.; Bearpark, M.; Heyd, J. J.; Brothers, E.; Kudin, K. N.; Staroverov, V. N.; Kobayashi, R.; Normand, J.; Raghavachari, K.; Rendell, A.; Burant, J. C.; Iyengar, S. S.; Tomasi, J.; Cossi, M.; Rega, N.; Millam, M. J.; Klene, M.; Knox, J. E.; Cross, J. B.; Bakken, V.; Adamo, C.; Jaramillo, J.; Gomperts, R.; Stratmann, R. E.; Yazyev, O.; Austin, A. J.; Cammi, R.; Pomelli, C.; Ochterski, J. W.; Martin, R. L.; Morokuma, K.; Zakrzewski, V. G.; Voth, G. A.; Salvador, P.; Dannenberg, J. J.; Dapprich, S.; Daniels, A. D.; Farkas, Ö.; Foresman, J. B.; Ortiz, J. V.; Cioslowski, J.; Fox, D. J., 2009.
20. F. Neese, *Wiley Interiscip. Rev.: Comput. Mol. Sci.*, 2011, **2**, 73-78.
21. F. Neese, *Wiley Interiscip. Rev.: Comput. Mol. Sci.*, 2017, **8**.
22. E. D. Hedegard, J. Kongsted and S. P. Sauer, *J. Chem. Theory Comput.*, 2013, **9**, 2380-2388.
23. M. Ernzerhof and G. E. Scuseria, *J. Chem. Phys.*, 1999, **110**, 5029-5036.
24. C. Adamo and V. Barone, *J. Chem. Phys.*, 1999, **110**, 6158-6170.
25. F. Weigend, *Phys. Chem. Chem. Phys.*, 2006, **8**, 1057-1065.
26. E. van Lenthe, J. G. Snijders and E. J. Baerends, *J. Chem. Phys.*, 1996, **105**, 6505-6516.
27. V. N. Staroverov, G. E. Scuseria, J. Tao and J. P. Perdew, *J. Chem. Phys.*, 2003, **119**, 12129-12137.
28. N. J. Stone, *Table of nuclear magnetic dipole and electric quadrupole moments. Atomic Data and Nuclear Data Tables*, 2005, **90**, 75-176.